Simple fits for the neutrino luminosities from protoneutron star cooling

Giuseppe Lucente[1,2,3,4,*], Malte Heinlein[5,6,†], Hans-Thomas Janka[5,‡] and Alessandro Mirizzi[1,2,§]

[1]*Dipartimento Interateneo di Fisica "Michelangelo Merlin," Via Amendola 173, 70126 Bari, Italy*
[2]*Istituto Nazionale di Fisica Nucleare—Sezione di Bari, Via Orabona 4, 70126 Bari, Italy*
[3]*Kirchhoff-Institut für Physik, Universität Heidelberg,*
Im Neuenheimer Feld 227, 69120 Heidelberg, Germany
[4]*Institut für Theoretische Physik, Universität Heidelberg, Philosophenweg 16,*
69120 Heidelberg, Germany
[5]*Max-Planck-Institut für Astrophysik, Karl-Schwarzschild-Strasse 1, 85748 Garching, Germany*
[6]*TUM School of Natural Sciences, Physics Department, Technische Universität München,*
James-Franck-Strasse 1, 85748 Garching, Germany

We propose a simple fit function, $L_{\nu_i}(t) = Ct^{-\alpha}e^{-(t/\tau)^n}$, to parametrize the luminosities of neutrinos and antineutrinos of all flavors during the protoneutron star (PNS) cooling phase at postbounce times $t \gtrsim 1$ s. This fit is based on results from a set of neutrino-hydrodynamics simulations of core-collapse supernovae in spherical symmetry. The simulations were performed with an energy-dependent transport for six neutrino species and took into account the effects of convection and muons in the dense and hot PNS interior. We provide values of the fit parameters C, α, τ, and n for different neutron star masses and equations of state as well as correlations between these fit parameters. Our functional description is useful for analytic supernova modeling, for characterizing the neutrino light curves in large underground neutrino detectors, and as a tool to extract information from measured signals on the mass and equation of state of the PNS and on secondary signal components on top of the PNS's neutrino emission.

I. INTRODUCTION

The neutrino signal from a future Galactic supernova (SN) explosion represents one of the next frontiers of neutrino astrophysics (see, e.g., Refs. [1–5]). Existing and planned large underground neutrino detectors guarantee that a high-statistics neutrino burst will be collected during such an event (see, e.g., Refs. [1,2,6–11]). This detection will be extremely important to probe the SN explosion mechanism [12–19], neutrino flavor conversions [20–24], and particle physics [24–26] occurring in the deepest stellar regions.

In order to characterize the response of a detector to a SN neutrino burst, one has to rely on the outcome of state-of-the-art numerical SN simulations. Different from the case of solar neutrinos, a standard prediction for SN neutrino fluxes does not exist. Therefore, many current studies employ a parametric approach with a suitable range of variation guided by the results of the simulations. For this purpose, it has been shown that the time-integrated SN

neutrino fluxes are well represented by a spectrum with the functional form [27,28]

$$f_\nu(E) \propto E^\beta e^{-(\beta+1)E/\langle E \rangle}, \qquad (1)$$

where $\langle E \rangle$ is the average energy of a given neutrino species.

Concerning the time evolution of the neutrino luminosities, most of the detector characterizations use, for comparison, results obtained from numerical tables provided by simulations (see, e.g., [1,8,29–32]). However, in order to extend parametric studies also to the temporal evolution of the neutrino signal, it would be useful to have a simple functional prescription also for the luminosities, based on a few parameters that permit one to cover the range of variation obtained in the numerical SN simulations.

In this respect, the seminal work of Loredo and Lamb [33], concerned with an analysis of SN 1987A data, assumed an exponential cooling model.[1] This simple recipe was often used (see, e.g., Refs. [35–37]) for schematic estimations. However, as noticed already in Ref. [38], protoneutron star (PNS) cooling calculations do not yield

---

[*]Contact author: lucente@thphys.uni-heidelberg.de
[†]Contact author: heinlein@mpa-garching.mpg.de
[‡]Contact author: thj@mpa-garching.mpg.de
[§]Contact author: alessandro.mirizzi@ba.infn.it

---

[1]A more sophisticated model accounting for both accretion and cooling phase was presented in Ref. [34].

exponential neutrino light curves but instead suggest that the neutrino luminosity is better described by a power-law decline [39]. A further step was taken in the recent work of Ref. [40], where on the grounds of an analysis of recent spherically symmetric PNS cooling simulations covering postbounce times up to $t \sim 70$ s, a combined ansatz of power-law and exponential behavior of the form $L_{\nu_i}(t) \propto t^{-1} e^{-(t/\tau)^n}$ was proposed for the long-time behavior of the neutrino light curve, where τ is a characteristic timescale of the PNS cooling.[2] In that work $\tau \sim 30$ s was adopted to handle the transition to the regime of neutrino transparency, and therefore the functional description of the neutrino light curve follows a simple decline according to t^{-1} in the first 10 s after core bounce. However, the models considered in Ref. [40] did not include the effect of convection in the PNS. This has important consequences for the shape of the neutrino light curve, because the Kelvin-Helmholtz neutrino cooling of the PNS is strongly accelerated if convection persists for many seconds.

In Ref. [42] it was shown that a kink in the neutrino light curve, when displayed in a doubly logarithmic form, signals the end of convection in the mantle layer of the PNS, while convection still continues in the deeper, high-density PNS core. The duration of PNS mantle convection and therefore the time of the kink depends on the nuclear equation of state (EOS), in particular, on the behavior of the nuclear symmetry energy as a function of the density at and above nuclear saturation. The kink is also present in the count rate of a neutrino detection and thus could be easily observed. When it occurs late during the PNS cooling, it resembles a "knee" since it is followed by a steep decline when the PNS cools off and gradually becomes transparent to neutrinos. Otherwise, the kink transitions into a longer, flatter tail of the light curve. Typically, in modern models the knee is witnessed to show up at $t < 10$ s [43,44].

Inspired by these previous findings, we perform a detailed analysis of the neutrino luminosities obtained in a set of spherically symmetric PNS cooling models recently described in Ref. [43]. These simulations were performed with six-species neutrino transport based on a fully energy-dependent two-moment scheme with a variable Eddington closure obtained from the solution of the Boltzmann transport equation. Moreover, the effects of PNS convection and muons were taken into account. After this analysis, we propose an accurate fit for the neutrino luminosities during the PNS cooling evolution at postbounce times $t \gtrsim 1$ s, based on the following functional form:

$$L_{\nu_i}(t) = C t^{-\alpha} e^{-(t/\tau)^n}, \qquad (2)$$

where the parameter C is a normalization constant, α describes the power-law behavior in the early cooling

phase, τ is a characteristic cooling time of the exponential drop at later times, and n determines the steepness of the exponential decline at these late times. Importantly, for models including PNS convection, the value of τ is much shorter, $\tau < 10$ s, than assumed in Ref. [40]. Therefore, this fit function can be useful as a sensitive probe of the presence and duration of convection in the PNS mantle during the long-time neutrino cooling. Such a probe is complementary to the method of analysis considered in Ref. [42], where the ratio of neutrino events at early and late times was proposed as a diagnostic measure.

In the present paper, we report our analysis and fitting procedure and provide extended tables with the parameter values for the fit functions of all our models and for interesting correlations between these fit parameters. The outline of the paper is as follows. In Sec. II we show the neutrino luminosities from our 1D PNS cooling simulations for different PNS masses and nuclear EOSs. In Sec. III we describe our analytical fitting of the neutrino and antineutrino luminosities of all flavors based on Eq. (2) for the models discussed before. In Sec. IV we discuss the dependence of the values of the fitting parameters on PNS mass and nuclear EOS and how their determination can help in deducing information on these latter quantities from a neutrino measurement. In Sec. V we discuss tight correlations of the parameter values, on the one hand, with the PNS mass (for fixed EOS) and, on the other hand, between each other (for fixed PNS mass). Then, in Sec. VI, we consider how the previous results change for models that neglect the effects of PNS convection and of muons in the PNS cooling models. In Sec. VII we show how our analytical recipe can be used to fit the event rate in a large neutrino underground detector. Finally, in Sec. VIII we discuss possible applications of our fitting formula and finish with conclusions. In several Appendixes we provide extended tables with the values obtained by our numerical fitting and needed for practical use.

II. NEUTRINO LUMINOSITIES

Our work is based on results from 1D hydrodynamical PNS cooling simulations employing the PROMETHEUS-VERTEX neutrino-hydrodynamics code [45], which solves the fully energy- and velocity-dependent neutrino transport for all six species of neutrinos and antineutrinos with a state-of-the-art implementation of the neutrino interactions [46–48]. The models we will use are taken from the Garching core-collapse supernova archive [49] (all data are available upon request) and they are the same as those considered in the recent study of Ref. [43], to which we refer the interested readers for more information on the model evolution and a discussion of the neutrino emission properties.

A concise and comprehensive summary of the physics inputs in the latest version of the PROMETHEUS-VERTEX code is also provided by Ref. [43]. In particular, the

---

[2]Analytical parametrizations of the late-time SN neutrino signal have been also presented in Ref. [41].

TABLE I.   Final times t_{fin} and ratios $X_{\nu_i}^{\text{fin}}$ [see Eq. (3)] for all PNS simulations and neutrino species. Values of $X_{\nu_i}^{\text{fin}}$ larger than 0.15 are printed in bold and asterisks mark the largest values, $X_{\nu_\mu}^{\text{fin}} = 0.219$ and $X_{\nu_\mu}^{\text{fin}} = 0.185$, for models 1.62-SFHx-c and for 1.61-LS220-c, respectively. The detailed numerical neutrino outputs for all the simulations listed here are available at the Garching core-collapse supernova archive [49].

Model	t_{fin} (s)	$X_{\nu_e}^{\text{fin}}$	$X_{\bar{\nu}_e}^{\text{fin}}$	$X_{\nu_\mu}^{\text{fin}}$	$X_{\bar{\nu}_\mu}^{\text{fin}}$	$X_{\nu_\tau}^{\text{fin}}$	$X_{\bar{\nu}_\tau}^{\text{fin}}$
1.36-DD2	8.69	0.023	0.015	0.013	0.012	0.011	0.011
1.36-SFHo	10.50	0.034	0.027	0.026	0.023	0.018	0.018
1.36-SFHx	10.06	0.059	0.054	0.060	0.056	0.046	0.045
1.36-LS220	12.36	0.078	0.065	0.075	0.067	0.064	0.062
1.44-DD2	13.72	0.004	0.002	0.002	0.002	0.002	0.002
1.44-SFHo	15.00	0.006	0.004	0.003	0.003	0.003	0.003
1.44-SFHx	11.72	0.027	0.022	0.020	0.018	0.014	0.014
1.44-LS220	14.84	0.031	0.024	0.029	0.024	0.020	0.019
1.62-DD2	10.75	0.013	0.008	0.007	0.006	0.006	0.006
1.62-SFHo	14.26	0.010	0.007	0.006	0.005	0.005	0.004
1.62-SFHx	13.45	0.020	0.016	0.014	0.013	0.010	0.009
1.62-LS220	13.58	0.123	0.111	0.115	0.107	0.115	0.112
1.77-DD2	11.26	0.015	0.009	0.009	0.008	0.007	0.007
1.77-SFHo	13.28	0.032	0.025	0.026	0.025	0.018	0.018
1.77-SFHx	13.91	0.030	0.026	0.025	0.024	0.017	0.017
1.77-LS220	16.33	0.082	0.073	0.090	0.083	0.093	0.090
1.93-DD2	12.81	0.009	0.005	0.006	0.005	0.005	0.004
1.93-SFHo	15.52	0.017	0.012	0.012	0.011	0.007	0.007
1.93-SFHx	16.38	0.016	0.013	0.011	0.010	0.007	0.007
1.93-LS220	19.95	0.037	0.034	0.048	0.045	0.053	0.051
1.62-DD2-c	13.95	0.040	0.022	0.028	0.025	0.023	0.022
1.62-SFHo-c	19.74	0.046	0.037	0.034	0.030	0.023	0.030
1.62-SFHx-c	18.75	**0.180**	**0.172**	**0.219***	**0.212**	**0.211**	**0.207**
1.61-LS220-c	20.92	**0.172**	0.146	**0.185***	**0.172**	**0.185**	**0.181**
1.62-DD2-m	9.58	0.014	0.009	0.009	0.008	0.009	0.008
1.62-SFHo-m	13.55	0.009	0.006	0.005	0.005	0.005	0.005

discussed models include a 1D treatment of PNS convection via a mixing-length description of the convective fluxes [2] and take into account the presence of muons in the hot PNS, including the corresponding muonic neutrino interactions [48], although the differences in the luminosities and spectra of μ and τ neutrinos turn out to be relatively small during most of the PNS cooling evolution (unless the PNS is very massive).

We consider simulations that yield baryonic PNS masses[3] of $1.36 M_\odot$, $1.44 M_\odot$, $1.62 M_\odot$, $1.77 M_\odot$, and $1.93 M_\odot$, in each case computed with four different nuclear EOSs, namely, DD2 [50–52], SFHo, SFHx [51,53], and LS220 with a nuclear incompressibility at saturation density of $K = 220$ MeV [54]. Correspondingly, we follow Ref. [43] in our naming convention of the simulations, specifying the PNS mass and the EOS in the model names, e.g., 1.62-DD2. Our

standard simulations include PNS convection and muons; those without convection are denoted by a suffix "-c" to their names and those without muons by a suffix "-m". In Table I, we list all of the discussed simulations and the final postbounce times t_{fin} when they were stopped.

In this work we are interested in the postaccretion phase of the PNSs born in core-collapse SNe, for which reason we focus on the evolution of the neutrino signal only at postbounce times $t \gtrsim 1$ s. The discussed PNS models result from 1D simulations with initial conditions from several 1D models of stellar progenitors with different precollapse masses. These models are artificially exploded at different instants after bounce, which are chosen such that the PNS mass after the end of the postbounce accretion attains the desired value. The neutrino-driven explosions are triggered by a sufficiently strong reduction of the density and thus of the ram pressure in the infall region upstream of the stalled SN shock (for more details, see Ref. [43]). Although it is common knowledge now that SN explosions are a 3D phenomenon and 3D simulations are needed to investigate the explosion mechanism and the postbounce accretion
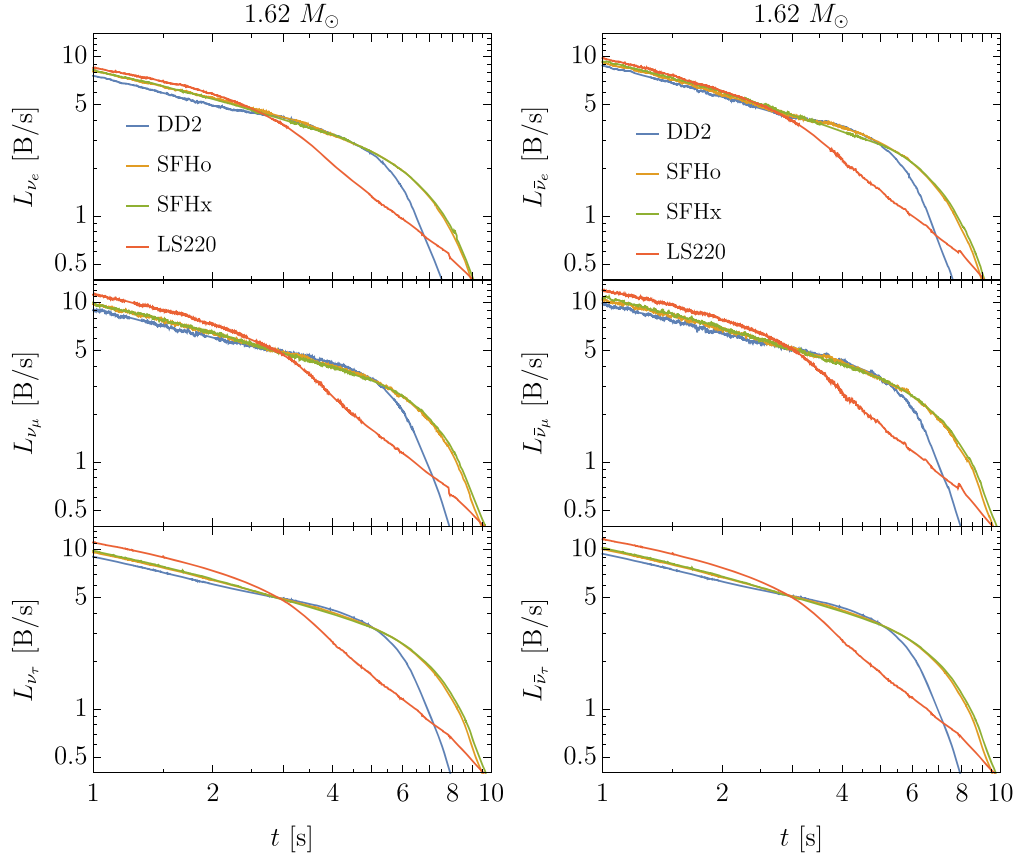
---

[3]Since the neutrino emission is tightly correlated with properties of the PNS, we use this quantity as reference for a systematic variation instead of the progenitor mass, which is not monotonically related with the PNS mass.

FIG. 1.   Time evolution of the luminosities L_{ν_i} for neutrinos (left) and antineutrinos (right) of all flavors for a PNS baryonic mass of $M_{\mathrm{NS}} = 1.62 M_\odot$ and all considered EOSs: DD2 (blue), SFHo (orange), SFHx (green), and LS220 (red).

phase as well as the associated neutrino signal, the late evolution times considered in our study, $t \gtrsim 1$ s, are sufficiently well represented by our 1D simulations if the PNS does not experience continued accretion that extends beyond 1 s after bounce. Another prerequisite is that our mixing-length treatment of PNS convection is a good approximation of the 3D hydrodynamics and associated energy and lepton transport that takes place inside the PNS over timescales of many seconds.

Figure 1 displays the time evolution of the luminosities $L_\nu(t)$ for all the neutrino (left panels) and antineutrino (right panels) flavors in units of B/s ($1B = 10^{51}$ erg) in the time interval [1,10] s for the $1.62 M_\odot$ models, computed with the set of considered EOSs cases: DD2 in blue, SFHo in orange, SFHx in green, and LS220 in red. From this figure, it is evident that the neutrino luminosities exhibit a change of their slope in the time interval considered. Since we expect a power-law behavior of the neutrino luminosities in the early cooling phase and we also want to enhance the visibility of the change in the steepness of the luminosity decline at later times, we take inspiration from Ref. [40] and show in Fig. 2 the product of the postbounce time and the luminosities, $tL_\nu(t)$, for all of the neutrino (left panels) and antineutrino (right panels) flavors in the same time interval and for the same simulations as in Fig. 1. One witnesses an interesting

difference of the results for the employed EOSs. For DD2, SFHo, and SFHx EOSs and all of the neutrino species, the quantity tL_ν increases as a power law at $t \gtrsim 1$ s to peak around $t \approx 4$ s, followed by a steep suppression at later times. This behavior produces a prominent knee at about 5–6 s after bounce. In contrast, for LS220 tL_ν reaches its peak earlier, namely, at $t \lesssim 3$ s, and it features a slower decline later on. Since for each model the luminosities of all heavy-lepton neutrino species show a similar evolution, we will focus exclusively on the $\bar{\nu}_\mu$ signal as representative of all nonelectron neutrino species, unless otherwise noted.

In order to compare the mass dependence for the different EOS cases, we show the time evolution of $tL_\nu(t)$ for the different PNS masses keeping the EOS fixed. Specifically, in Fig. 3 we consider the results for DD2 (left) and SFHo (right), and in Fig. 4 we present those for SFHx (left) and LS220 (right). In each panel, the $1.36 M_\odot$ (blue), $1.44 M_\odot$ (orange), $1.62 M_\odot$ (green), $1.77 M_\odot$ (red), and $1.93 M_\odot$ (purple) models are plotted for ν_e (top), $\bar{\nu}_e$ (middle), and $\bar{\nu}_\mu$ (bottom). It is obvious that, at fixed time t, the luminosity becomes larger as the PNS mass increases. This dependence is similar for all EOSs and all neutrino species. Additionally, the maximum of tL_ν is shifted to later times and the subsequent decline starts correspondingly later for higher PNS masses. These findings, which are
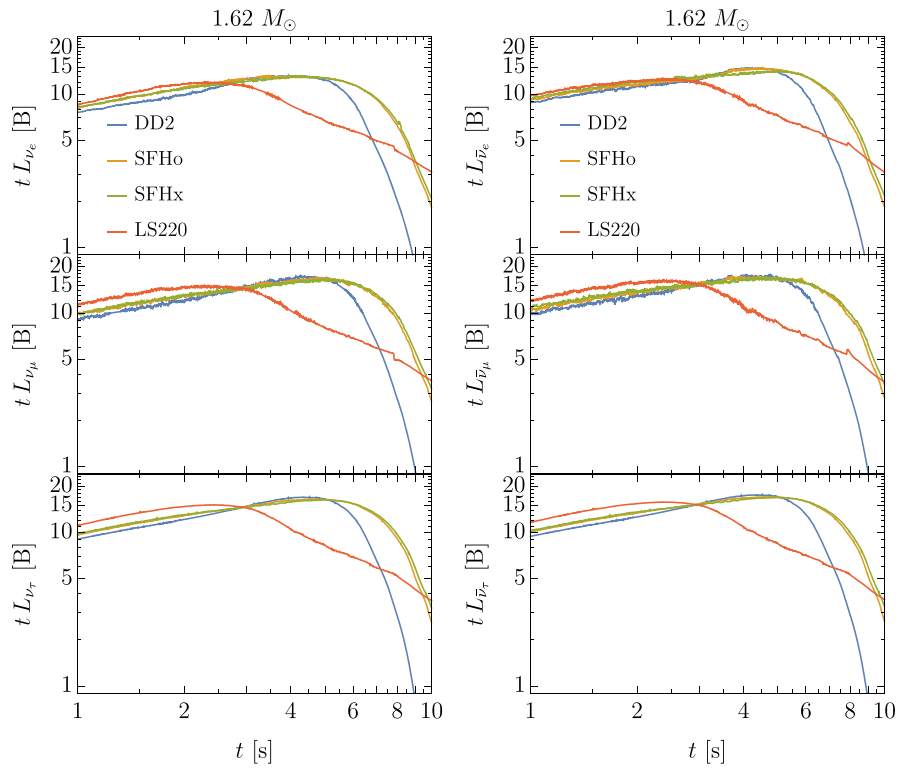
FIG. 2. Time evolution of the product of time and luminosities, tL_{ν_i}, for neutrinos (left) and antineutrinos (right) of all flavors for $M_{NS} = 1.62M_\odot$ and all considered EOSs: DD2 (blue), SFHo (orange), SFHx (green), and LS220 (red).

FIG. 3. Time evolution of the product of time and luminosity, tL_{ν_i}, for ν_e (upper), $\bar{\nu}_e$ (middle), and $\bar{\nu}_\mu$ (lower) for DD2 (left) and SFHo (right) and all investigated PNS masses: $M_{NS} = 1.36M_\odot$ (blue), $M_{NS} = 1.44M_\odot$ (orange), $M_{NS} = 1.62M_\odot$ (green), $M_{NS} = 1.77M_\odot$ (red), and $M_{NS} = 1.93M_\odot$ (purple).
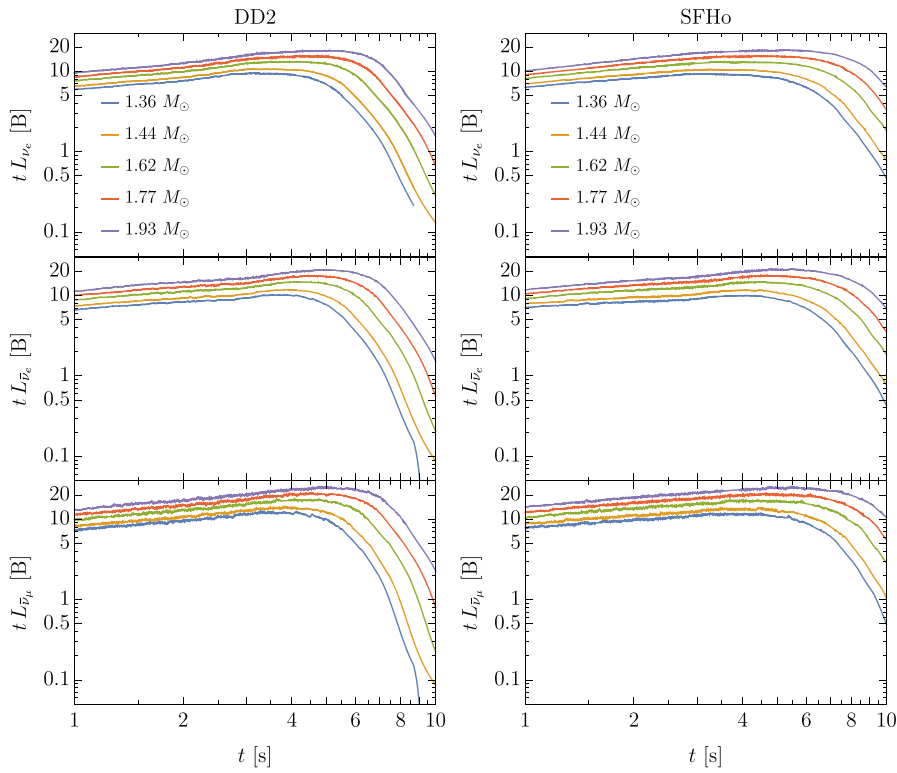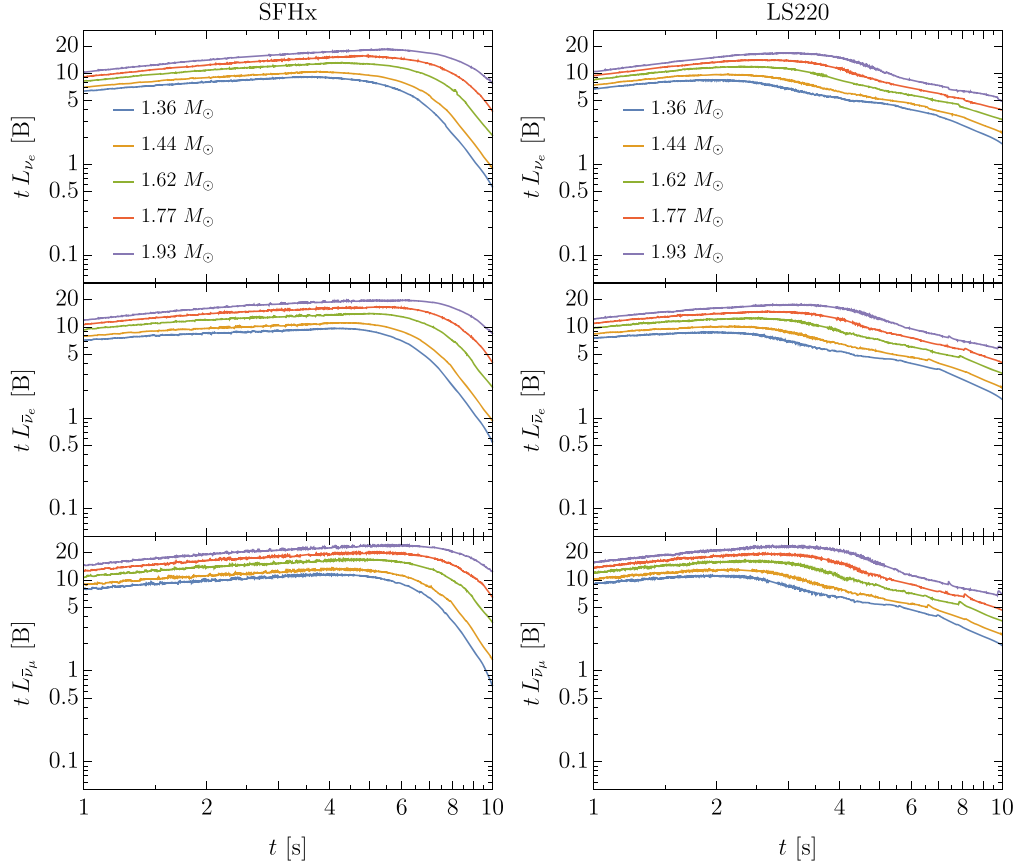
FIG. 4. Time evolution of the product of time and luminosity, tL_{ν_i}, for ν_e (upper), $\bar{\nu}_e$ (middle), and $\bar{\nu}_\mu$ (lower) for SFHx (left) and LS220 (right) and all investigated PNS masses: $M_{\rm NS} = 1.36M_\odot$ (blue), $M_{\rm NS} = 1.44M_\odot$ (orange), $M_{\rm NS} = 1.62M_\odot$ (green), $M_{\rm NS} = 1.77M_\odot$ (red), and $M_{\rm NS} = 1.93M_\odot$ (purple).

consistent with multi-D results in [17], can be explained by the fact that more gravitational binding energy is released in neutrinos when the PNS has a bigger mass.

For each case shown in Figs. 2–4, the quantity tL_ν has a peak at $t_{\nu_i,{\rm max}} \lesssim 6$ s, when we define $L_{\nu_i,{\rm max}} \equiv L_{\nu_i}(t_{\nu_i\,{\rm max}})$. The corresponding values of $t_{\nu_i,{\rm max}}$ are listed in Table II for neutrinos and in Table III for antineutrinos in Appendix A. In Table I, we provide the values of the quantity

$$X_{\nu_i}^{\rm fin} \equiv \frac{t_{\rm fin}L_{\nu_i,{\rm fin}}}{t_{\nu_i,{\rm max}}L_{\nu_i,{\rm max}}}, \tag{3}$$

which is a measure for how long our simulations followed the late-time luminosity decline until they were stopped at $t_{\rm fin}$. For our benchmark PNS models (all models including muons and convection), $X_{\nu_i}^{\rm fin} \lesssim 0.15$ holds for all neutrinos and antineutrinos (the largest value is $X_{\nu_e}^{\rm fin} = 0.123$ for 1.62-LS220). In order to adopt a well-defined, common final time for all of the neutrino species and simulations when fitting the luminosities in the following, we cut the data at an instant $t_{\nu_i,c}$ when $X_{\nu_i}^{\rm c} \equiv t_{\nu_i,c}L_{\nu_i,c}/(t_{\nu_i,{\rm max}}L_{\nu_i,{\rm max}}) = 0.15$. In addition to the values of $t_{\nu_i,{\rm max}}$, we also provide

those of $t_{\nu_i,c}$ for all neutrino species and simulations in Tables II and III in Appendix A. It can be seen that for a fixed EOS and neutrino species, the values of both of these quantities increase with the PNS mass. In contrast, given the PNS mass and EOS, $t_{\nu_i,{\rm max}}$ and $t_{\nu_i,c}$ do not vary much among the different kinds of neutrinos and antineutrinos (e.g., for 1.62-DD2 $t_{\nu_i,{\rm max}} \approx 4$ s and $t_{\nu_i,c} \approx 8$ s for all species). However, at fixed PNS mass, $t_{\nu_i,{\rm max}}$ and $t_{\nu_i,c}$ feature a strong dependence on the considered EOS. In particular, $t_{\nu_i,c} \lesssim 10$ s for all the benchmark models with DD2, whereas SFHo and SFHx lead to slightly larger values of $t_{\nu_i,c}$, with $t_{\nu_i,c} \lesssim 12.5$ s for all models, and in the cases with LS220 we find the highest values of $t_{\nu_i,c}$, with $t_{\nu_i,c} \lesssim 15$ s for the largest PNS mass.

III. FIT FUNCTIONS

After an analysis of the models described above, we propose Eq. (2) as fit function for the neutrino luminosities in the considered time window,
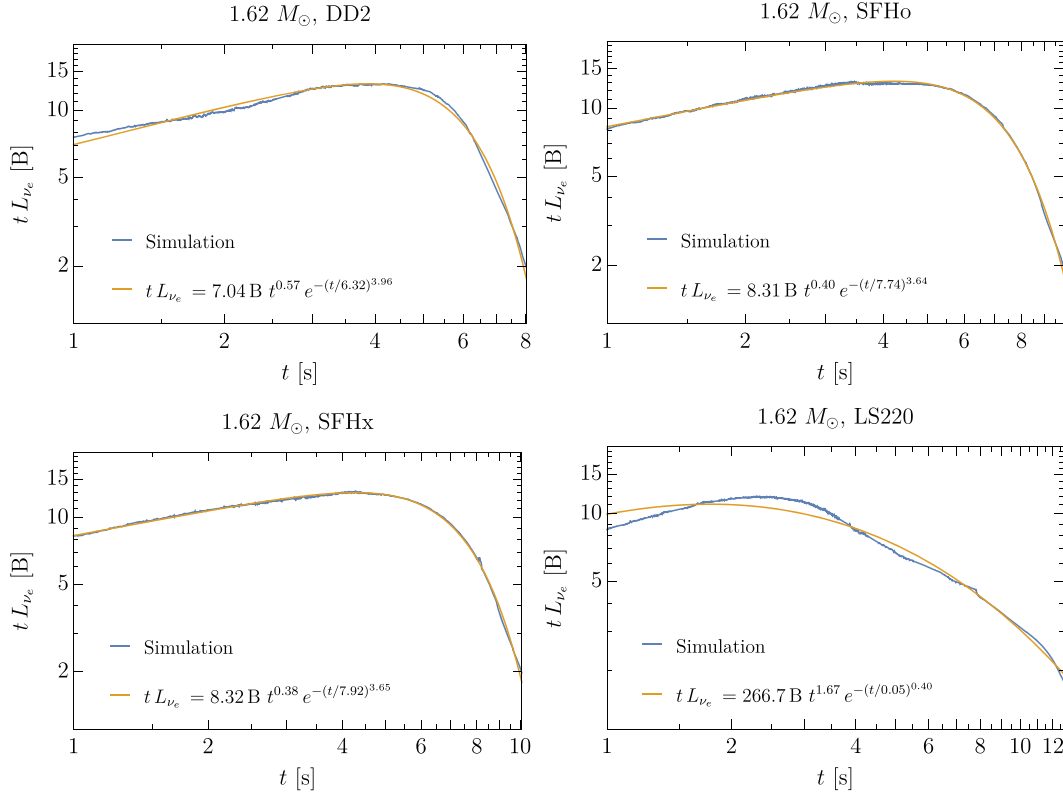
$$L_{\nu_i}(t) = Ct^{-\alpha}e^{-(t/\tau)^n},$$

FIG. 5.   Time evolution between 1 s and $t_{\nu_e,\mathrm{c}}$ of the product of time and ν_e luminosity, tL_{ν_e}, for simulation data (blue) and their fits (orange) for $M_{\mathrm{NS}} = 1.62 M_\odot$ and different EOSs: DD2 (upper left), SFHo (upper right), SFHx (lower left), and LS220 (lower right).

where C, α, τ, and n are free parameters and t and τ are measured in seconds.[4] In Eq. (2) the parameter C is a normalization constant, α describes the power-law behavior at early cooling time deviating from the simple t^{-1} behavior, τ is a characteristic cooling time for the exponential drop after the peak in tL_ν, with n representing the strength of the suppression at late times. We mention here that at the moment there is no straightforward argument explaining the power-law behavior at early cooling time, given that PNS convection plays an important role and it cannot be treated in simple ways. As an example, we show for the $1.62 M_\odot$ model and all EOSs the time evolution of tL_{ν_i} from simulations (blue lines) and its best fit (orange) between $t = 1$ s and $t_{\nu_i,\mathrm{c}}$, for ν_e in Fig. 5, for $\bar{\nu}_e$ in Fig. 6, and for $\bar{\nu}_\mu$ in Fig. 7. For DD2, SFHo, and SFHx the fit well reproduces the results from the simulations in the considered time interval, with best-fit parameters in a similar range. For each EOS, the highest values of the fit parameters C and τ are obtained for $\bar{\nu}_\mu$, while ν_e show the lowest ones. A similar behavior is found for the other PNS masses.

The fit for models with EOS LS220 shows worse agreement with the data from simulations (see the lower right

panels in Figs. 5–7). In particular, for all neutrino species the fit overestimates the luminosity at $t \approx 1$ s and exhibits a lower value of the peak, whereas it well reproduces the luminosity at later times. In this case, the values of the best-fit parameters are in a completely different range compared to those of the models with the other EOSs. In particular, for each neutrino species $C \approx \mathcal{O}(100)$ B/s and $\alpha < 0$, whereas τ and n adopt much smaller values than for the other considered EOSs, with $\tau \lesssim 0.1$ s and $n \lesssim 0.5$, due to the more shallow decline of the luminosity at late times. The differences in the time dependence of the neutrino luminosities between models with different EOSs can be understood by the different behavior of the nuclear symmetry energy as a function of baryon density for the considered EOS. In the LS220 EOS, the symmetry energy exhibits a steeper increase with baryon density than in all other cases. As discussed in Ref. [42], a larger positive derivative of the symmetry energy with baryon density can lead to suppressed convection in the PNS mantle at high densities and low electron fraction. This effect happens in the simulations with the LS220 EOS after about 3 s and gradually quenches PNS mantle convection, thus delaying subsequent PNS neutrino cooling due to reduced neutrino luminosities. In contrast, PNS convection continues to be active in a spatially more extended region including the PNS mantle in simulations with the other three EOSs, for which reason convectively enhanced neutrino luminosities are maintained for a longer period of time until a

---

[4]We define the general parameters as C, α, τ, and n and we use C_{ν_i}, α_{ν_i}, τ_{ν_i}, and n_{ν_i} when referring specifically to a neutrino species ν_i.

FIG. 6. Time evolution between 1 s and $t_{\bar{\nu}_e,c}$ of the product of time and $\bar{\nu}_e$ luminosity, $tL_{\bar{\nu}_e}$, for simulation data (blue) and their fits (orange) for $M_{NS} = 1.62M_\odot$ and different EOSs: DD2 (upper left), SFHo (upper right), SFHx (lower left), and LS220 (lower right).
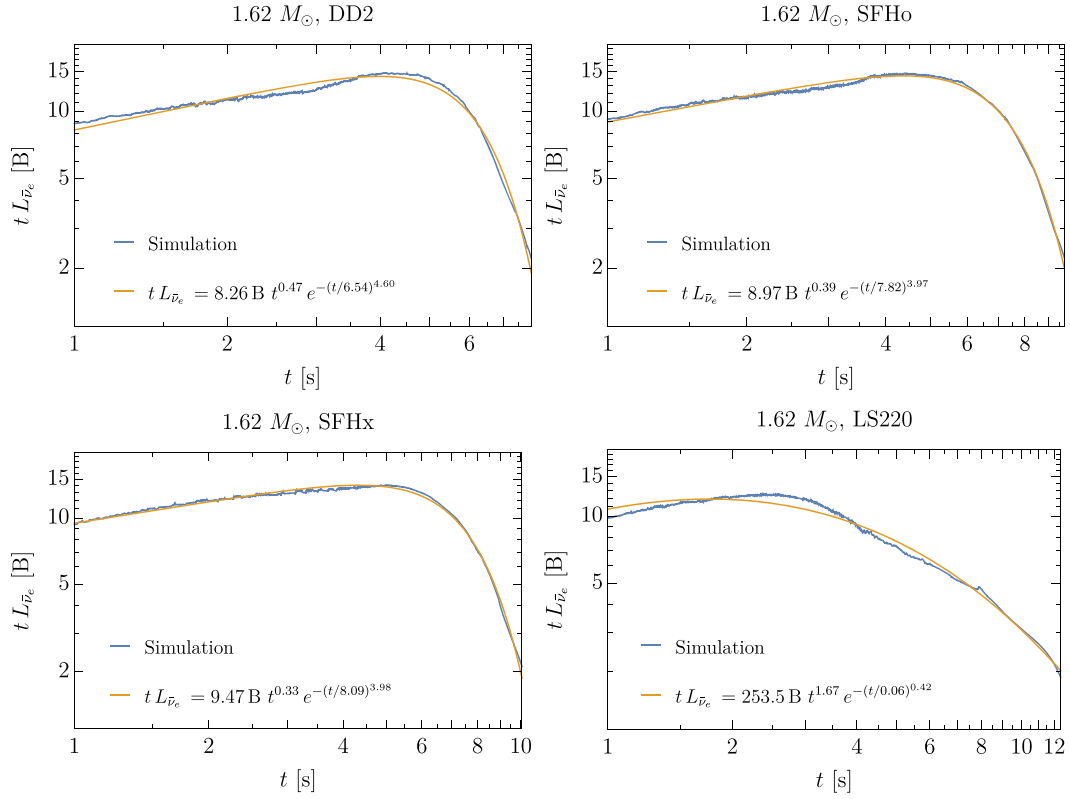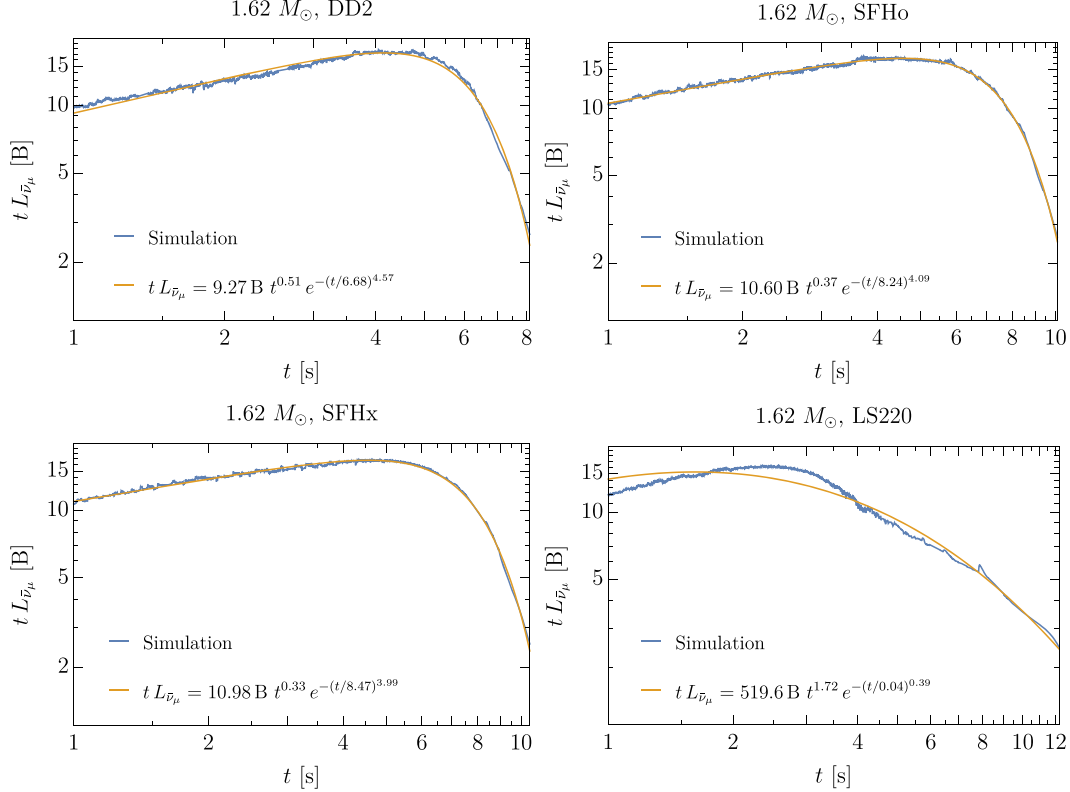

FIG. 7. Time evolution between 1 s and $t_{\bar{\nu}_\mu,c}$ of the product of time and $\bar{\nu}_\mu$ luminosity, $tL_{\bar{\nu}_\mu}$, for simulation data (blue) and their fits (orange) for $M_{NS} = 1.62M_\odot$ and different EOSs: DD2 (upper left), SFHo (upper right), SFHx (lower left), and LS220 (lower right).
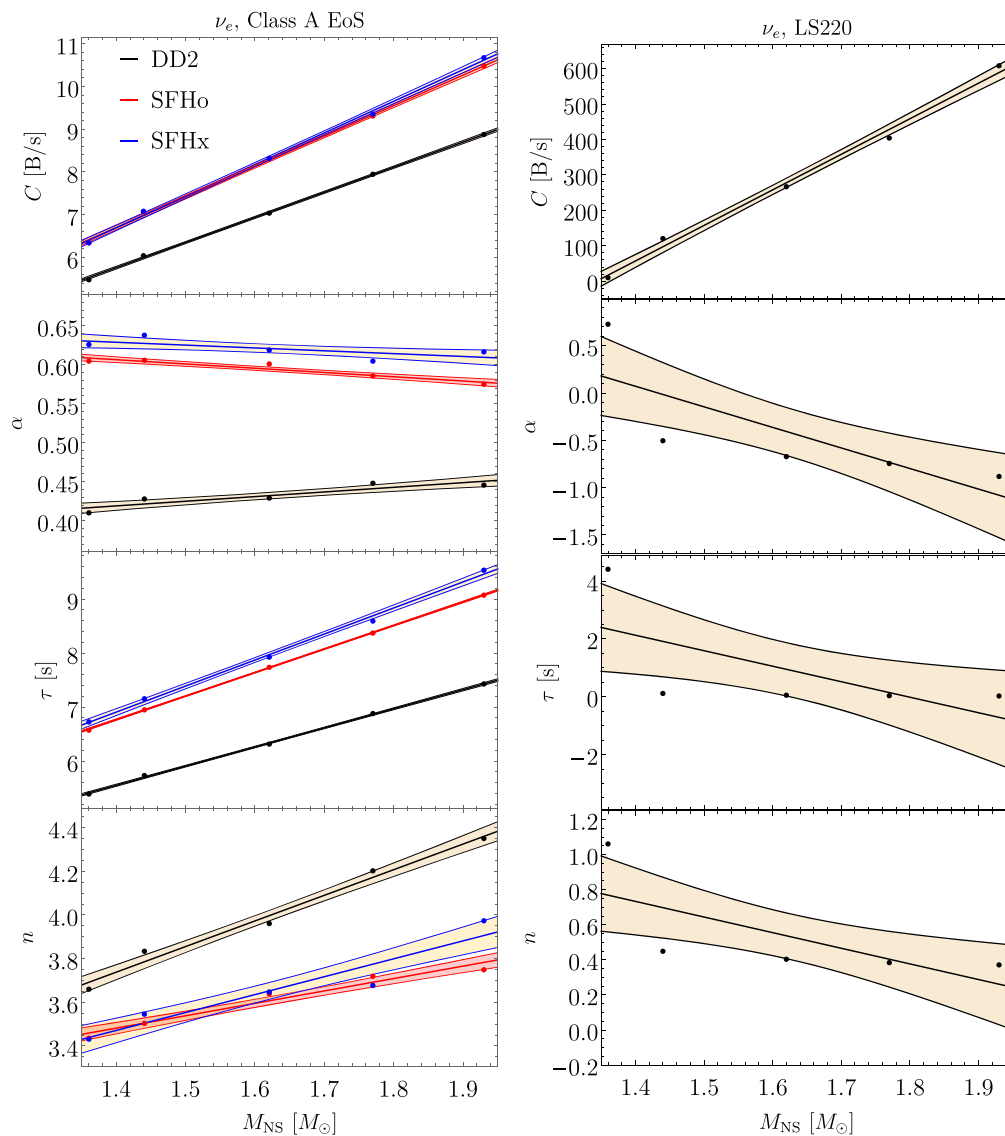
FIG. 8.   Best-fit parameters C, α, τ, and n as functions of the PNS mass for ν_e for class A EOSs (left) and for LS220 (right), obtained with data between 1 s and $t_{\nu_e,c}$. The shaded areas represent the 1σ confidence bands.

late, steep decline follows when the PNS has deleptonized and cools off. These differences explain the early kink in the neutrino luminosities for models with the LS220 EOS, whereas a prominent kneelike shape of $L_\nu(t)$ can be witnessed for the DD2, SFHo, and SFHx models (see Fig. 1). These differences motivate us to define DD2, SFHo, and SFHx as members of an EOS class that we call "class A," whereas LS220 is a representative of a "class B." The parameters of the symmetry energies for all the EOS cases used in our study are listed in Table XII in Appendix F.

In Appendix B we report the values of the best-fit parameters and their 1σ uncertainties,[5] for neutrinos and antineutrinos of all flavors and all considered models with

different PNS masses and EOSs. For each species, the 1σ errors on the best-fit parameters are within $\sim\mathcal{O}(0.1\text{--}1)\%$ for class A EOSs, whereas for LS220 the maximum errors are $\sim\mathcal{O}(10)\%$ or even larger, and tend to increase at higher PNS masses, reflecting the lower quality of the fit.

IV. DEPENDENCE ON PNS MASS AND EQUATION OF STATE

The best-fit parameters are plotted as functions of the PNS mass in Fig. 8 for ν_e, in Fig. 9 for $\bar{\nu}_e$, and in Fig. 10 for $\bar{\nu}_\mu$, separately for class A EOSs in the left panels and the LS220 case of class B in the right panels.

A. Class A EOS

For class A EOSs and all species of neutrinos and antineutrinos, the behavior of all of the fitting parameters

---

[5]The best-fit values and errors are obtained with Nonlinear-ModelFit function in *Mathematica*.
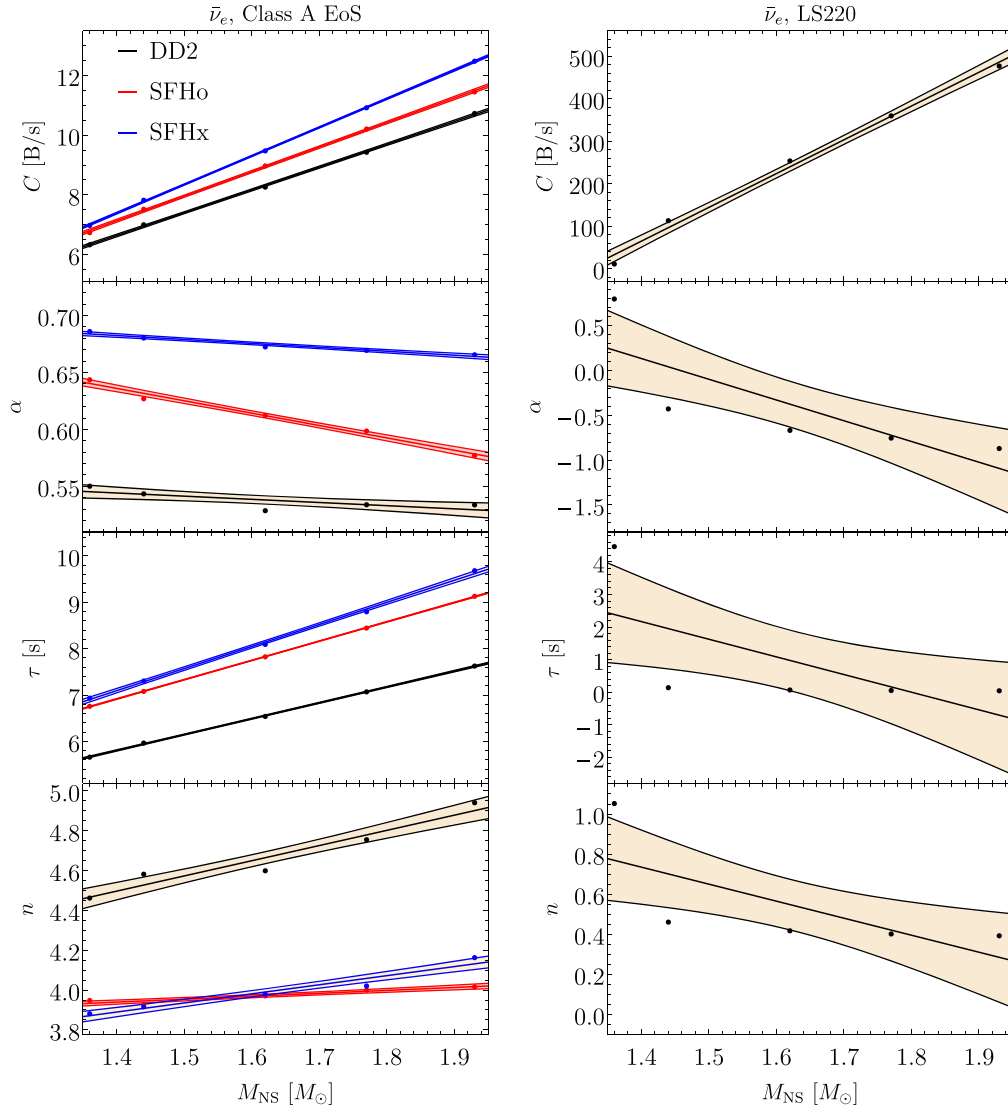
FIG. 9. Best-fit parameters C, α, τ, and n as functions of the PNS mass for $\bar{\nu}_e$ for class A EOSs (left) and for LS220 (right), obtained with data between 1 s and $t_{\bar{\nu}_e,c}$. The shaded areas represent the 1σ confidence bands.

can be well reproduced with linear dependences on the PNS mass, as shown by the black (DD2), red (SFHo), and blue (SFHx) lines in the left panels of Figs. 8–10. The shaded area around the linear interpolation represents the 1σ confidence band for each linear fit, obtained from the standard mean square uncertainties associated with the linear regression. In Table VIII of Appendix C we provide the best-fit parameter values that describe the linear dependencies of the fitting parameters C, α, τ, and n on the PNS mass for all neutrino and antineutrino species and all of the considered EOS.

(i) The "normalization parameter C" (top panels) adopts values of $5B/s \lesssim C \lesssim 15$ B/s for all neutrino species and it increases with the PNS mass. In particular, DD2 leads to the lowest values and SFHo and SFHx feature a similar dependence, with SFHx providing the largest values of C.

(ii) The "power-law index" α (second panels from top) shows a mild dependence on the PNS mass, featuring values of $0.50 \lesssim \alpha \lesssim 0.70$ for all neutrino species, with an increase in the case of DD2 and a slight decrease for SFHo and SFHx. Similar to the normalization parameter, for each kind of neutrino and PNS mass, the largest value of α is obtained with SFHx and the smallest one with DD2.

(iii) The "late-time suppression parameters" τ and n (third and fourth panels from top) tend to increase with the PNS mass for all neutrino species, with values of 5 s $\lesssim \tau \lesssim 10$ s and $3 \lesssim n \lesssim 5$. In particular, for all neutrino kinds and PNS masses, DD2 leads to the lowest values of τ and SFHx to the largest ones. On the other hand, DD2 yields the largest n values for ν and $\bar{\nu}$ of all flavors and all PNS masses, whereas the 1σ confidence bands of n for
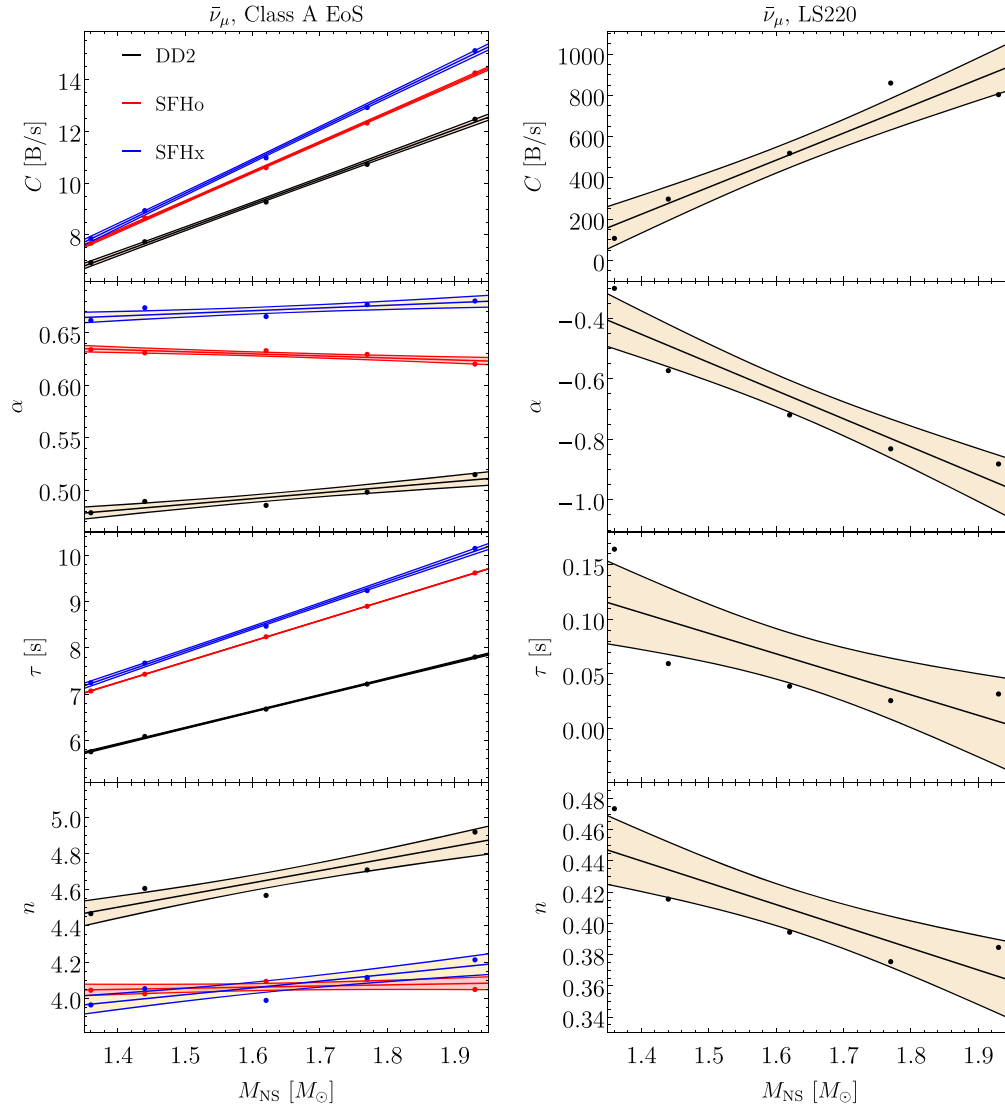
FIG. 10.   Best-fit parameters C, α, τ, and n as functions of the PNS mass for $\bar{\nu}_\mu$ for class A EOSs (left) and for LS220 (right), obtained with data between 1 s and $t_{\bar{\nu}_\mu, c}$. The shaded areas represent the 1σ confidence bands.

SFHo and SFHx models overlap in the mass range of $1.4 M_\odot \lesssim M_{\mathrm{NS}} \lesssim 1.7 M_\odot$, with SFHx showing larger values of n than SFHo at higher PNS masses.

A given value of C, τ, and n can be obtained with different combinations of EOS and neutron star (NS) mass. For instance, for $\bar{\nu}_e$, $\tau = 7$ s corresponds to $M_{\mathrm{NS}} \approx 1.38 M_\odot$ and SFHx, $M_{\mathrm{NS}} \approx 1.45 M_\odot$ and SFHo, as well as $M_{\mathrm{NS}} \approx 1.77 M_\odot$ and DD2. However, the best-fit values of α lie in different ranges for different EOSs. For instance, $0.6 \lesssim \alpha_{\bar{\nu}_e} \lesssim 0.65$ would point to the SFHo EOS, irrespective of the PNS mass. Therefore, in the case of a future observation of a SN neutrino signal, the measurement of α would provide information on the EOS and the PNS mass and, combined with the measurements of the other fit parameters, would allow us to characterize the PNS mass and the EOS. More explicitly, neglecting for

simplicity flavor mixing, a combined measurement of $\tau = 7$ s, $\alpha \approx 0.63$, and $n \approx 3.9$ for the $\bar{\nu}_e$ luminosity would suggest a SN explosion leading to a PNS of mass $1.44 M_\odot$, whose interior properties are described by the SFHo EOS. As further discussed in Sec. VII, due to the similarities of the spectra and luminosities of electron antineutrinos and heavy-lepton antineutrinos in our models at times $t \gtrsim 1$ s, flavor conversions are not a major effect, although they would make the reconstruction of the fit parameters less straightforward, but without spoiling our result. The accurate reconstruction of the parameters is left for future work.

B. LS220 EOS

A different discussion is required by the LS220 models. In this case, as shown in the right panels of Figs. 8–10 and

in Table VIII of Appendix C, the lower quality of the fit leads to a slightly different dependence of the fit parameters on the PNS mass.

   (i) The normalization parameter C (top panels) is $C \sim O(10\text{--}1000)$ B/s for all of the neutrino species and it increases linearly with the PNS mass.

   (ii) The power-law index α (second panels from top) tends to decrease as the PNS mass increases. It is negative for all models and neutrino species except for ν_e and $\bar{\nu}_e$ in the simulation with $M_{NS} = 1.36 M_\odot$, where $\alpha > 0$.

   (iii) The late-time suppression parameters τ and n (third and fourth panels from top) tend to decrease with higher PNS mass. For the 1.36-LS220 model, we get $\tau \sim 4$ s and $n > 1$ for ν_e and $\bar{\nu}_e$ (see Table V in Appendix B), whereas $\tau \lesssim 0.25$ s and $n \lesssim 0.5$ in all the other cases (Tables VI and VII).

Even though the linear interpolations of the mass dependence have a lower quality for the LS220 EOS, the best-fit parameters for this EOS possess values in completely different ranges than for the class A EOSs. Thus, the observation of such values would clearly point to a class B EOS for the PNS in the discovered SN.

V. CORRELATION BETWEEN τ AND α

Since the fit parameters of all class A EOSs have values in similar ranges, it is useful to search for possible relations between them. We disregard the case of LS220 here, because its parameter values lie in completely different regimes. For fixed PNS mass and given EOS, we find that the power-law index α and the suppression time τ for the class A EOSs exhibit correlations that can be fairly well described by linear functions,

$$\tau(s) = A + B\alpha, \qquad (4)$$

for all neutrino species except $\bar{\nu}_e$. This is shown in Fig. 11 for neutrinos (left) and antineutrinos (right) of all flavors and all class A EOSs. In Appendix D, in Table IX we report the best-fit values with errors obtained from linear regression for A and B for all neutrino species. The pairs of values (τ, α) are represented by filled circles for the DD2 EOS, filled squares for SFHo, and filled diamonds for SFHx in Fig. 11. Different colors correspond to the different PNS masses: black for $M_{NS} = 1.36 M_\odot$, red for $M_{NS} = 1.44 M_\odot$, blue for $M_{NS} = 1.62 M_\odot$, green for $M_{NS} = 1.77 M_\odot$, and orange for $M_{NS} = 1.93 M_\odot$.

As a general trend for fixed NS mass, SFHx leads to the largest values of τ and α for ν and $\bar{\nu}$ of all flavors, whereas DD2 yields the smallest values of τ and α. The linear increase of τ as a function of α could be understood in simple terms by the fact that a larger value of α causes a faster decline of the luminosity in the first seconds, and therefore, if the initial luminosity (i.e., specifically at 1 s

in our context) were the same, less energy is carried away by neutrinos during this early power-law phase of the luminosity. Thus, if the total energy released in neutrinos were fixed, one would expect that a higher value of α leads to a stretching of the subsequent exponential luminosity decrease with a final drop only at later times, implying a larger τ. Although this explanation sounds plausible, it is an oversimplification of the real situation. First, at $t = 1$ s the luminosities are not the same for a given PNS mass, but smallest for DD2 and largest for SFHx (see Fig. 1). Second, also the total energy (individually for all neutrino species as well as summed up) is different, namely, smallest for DD2 and largest for SFHx (see Tables I and VII in [43]), which correlates with the final gravitational binding energy of the cold NS (but not strictly with the final NS radius, which is largest for models with the DD2 EOS and smallest with SFHo when $M_{NS} \gtrsim 1.2 M_\odot$). The true reasons for the tight correlation between α and τ values are therefore more subtle than suggested by the simple argument given above.

Moreover, the quality of the linear relation, Eq. (4), differs between different neutrino species. Figure 11 and the values of the coefficients A and B in Table IX in Appendix D reveal that the linear relation works better for neutrinos than for antineutrinos. The good quality of the linear fit especially for ν_e could be useful to disentangle the NS mass and EOS with a measured pair of values (τ, α). In this context, it should be mentioned that the linear fits for $\bar{\nu}_e$ are considerably worse than for all other neutrino species (upper right panel in Fig. 11); the 1σ confidence bands display substantial overlap in the whole range of α values. In contrast, the linear fit function works better for the antineutrinos of the nonelectron flavors, with $\bar{\nu}_\tau$ (bottom right panel) showing slightly narrower 1σ confidence bands than $\bar{\nu}_\mu$ (middle right panel). The reason for the particularly poor quality of the linear fit for $\bar{\nu}_e$ is the relatively wide separation of the α values for the SFHo and SFHx EOSs, in contrast to ν_e, where the corresponding values are very close to each other and the linear fit is very good. The lower quality of linear $\tau - \alpha$ relations for the heavy-lepton neutrinos also confirms this general tendency that such a fit function is less suitable to describe the correlation of both parameters when the distance between α for SFHo and SFHx grows. This leaves the possibility that the linear function works well for ν_e just because of favorable properties of the SFHo and SFHx EOSs. More investigation with larger sets of different nuclear EOS cases is therefore required before one can rely on the validity of linear $\tau - \alpha$ relations.

VI. IMPACT OF MUONS AND CONVECTION

In order to assess the impact of some of our physics inputs of the simulations, we investigate additional PNS cooling calculations for a PNS mass of $1.62 M_\odot$ now, where we either omitted convection or muons. Nonconvective
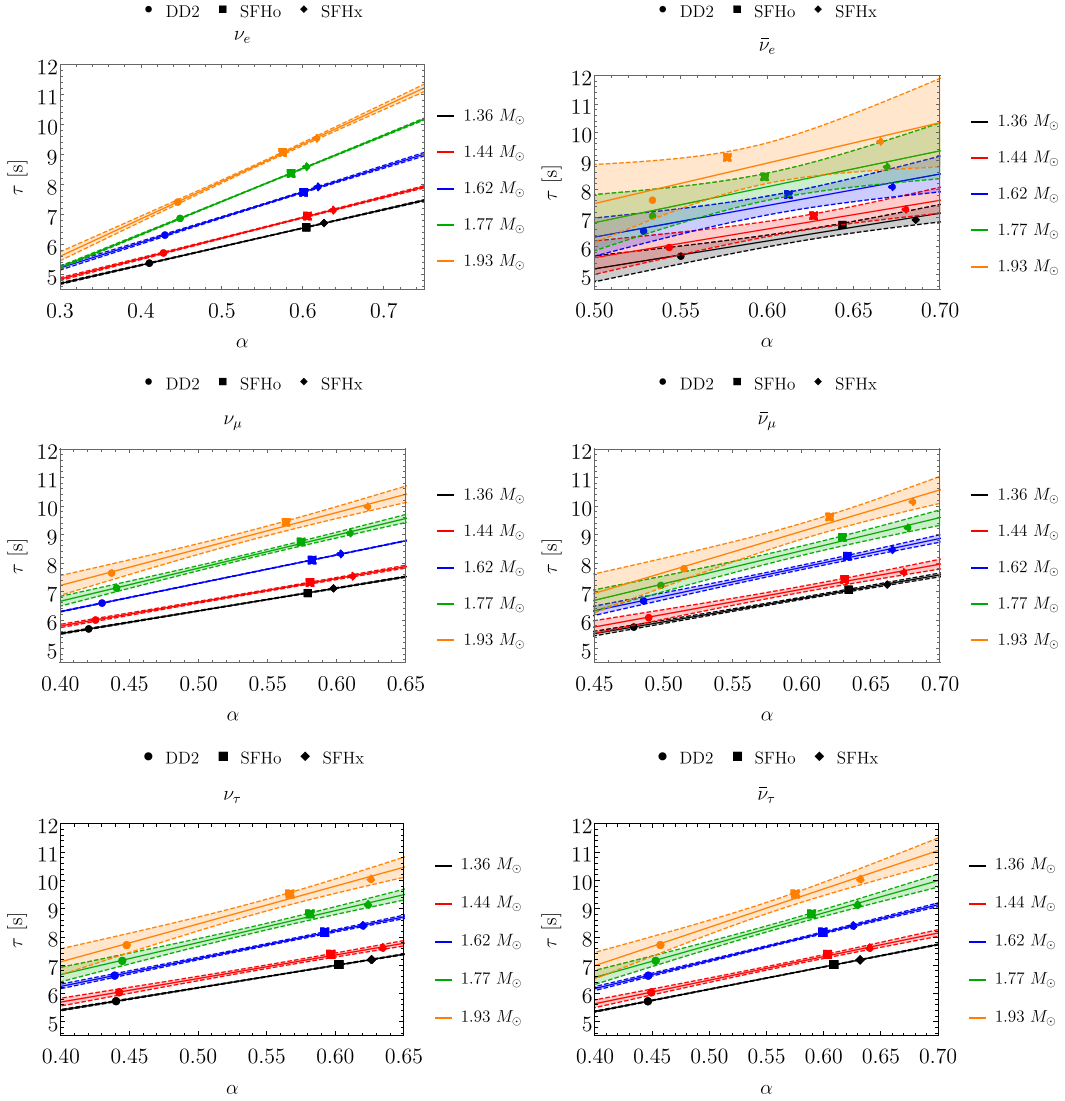
FIG. 11. Correlations of the fitting parameters τ (in units of seconds) and α for ν_e (top left), $\bar{\nu}_e$ (top right), ν_μ (central left), $\bar{\nu}_\mu$ (central right), ν_τ (bottom left), $\bar{\nu}_\tau$ (bottom right), for all case A EOSs and all considered PNS masses, obtained from simulation output data between 1 s and $t_{\nu_i,c}$ for each neutrino species ν_i.

models were computed for all considered EOSs and are denoted by a suffix -c appended to their names (e.g., 1.62-DD2-c), whereas only two models are considered without muons (suffix -m), namely, 1.62-DD2-m and 1.62-SFHo-m [49]. The bottom two data blocks of Table I provide the final simulation times and the corresponding reduction factors $X_{\nu_i}^{\text{fin}}$ for all neutrino species in these additional models. Bold numbers in Table I for models 1.62-SFHx-c and 1.61-LS220-c signal that the simulations were stopped when $X_{\nu_i}^{\text{fin}} > 0.15$, implying that for these models our standard cutoff time $t_{\nu_i,c}$ is larger than t_{fin}. In both of the simulations, the weakest suppression is obtained for ν_μ, with $X_{\nu_\mu}^{\text{fin}} = 0.219$ for 1.62-SFHx-c and $X_{\nu_\mu}^{\text{fin}} = 0.185$ for 1.61-LS220-c (see the values marked by a star in Table I).

Therefore, to test the impact of convection for the SFHx and LS220 EOSs, we cut our luminosity data at $t_{\nu_i,\text{Co}}$, when $X_{\nu_i}^{\text{Co}} = t_{\nu_i,\text{Co}} L_{\nu_i,\text{Co}} / t_{\nu_i,\text{max}} L_{\nu_i,\text{max}} = 0.22$ for simulations with SFHx and $X_{\nu_i}^{\text{Co}} = 0.19$ for simulations with LS220. The values of $t_{\nu_i,\text{Co}}$ for all neutrino species of these simulations are given in Table IV of Appendix A.

Figure 12 presents neutrino and antineutrino signals at $t > 1$ s for the mentioned $M_{\text{NS}} = 1.62 M_\odot$ simulations with modified input physics and the different EOS previously considered. The left panels display the results for our models without convection in the time interval [1,20] s, whereas the right panels show our cases without muons in the time interval [1,10] s, for ν_e (upper panels), $\bar{\nu}_e$ (central), and $\bar{\nu}_\mu$ (lower).

FIG. 12. Time evolution of the product of time and luminosity, tL_{ν_i}, for ν_e (top), $\bar{\nu}_e$ (middle), and $\bar{\nu}_\mu$ (bottom) for a simulations without convection (left) and without muons (right), wi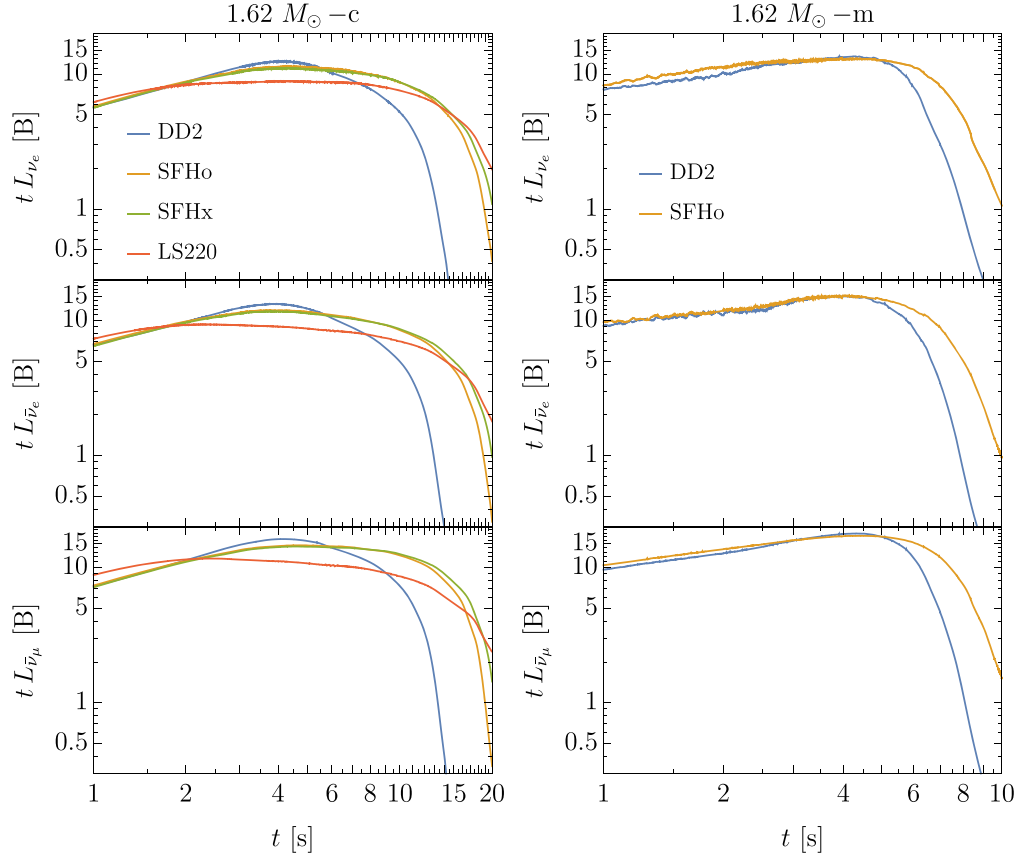th $M_{NS} = 1.62 M_\odot$ and different EOS: DD2 (blue), SFHo (orange), SFHx (green), and LS220 (red). Simulations using SFHx and LS220 without muons are not available.

In the absence of convection, the quantity tL_ν declines steeply only at $t \gtrsim 10$ s for all neutrino species, with different characteristic features depending on the EOS (see the second data block from the bottom of Tables II and III in Appendix A). In particular, we witness the following:

(i) DD2 (blue lines) has the shortest cooling time, with tL_ν peaking at $t \approx 4$ s and being reduced by a factor 0.15 of the maximum values at $t \approx 12$ s.

(ii) SFHo (orange lines) shows a peak of tL_ν at $t \approx 4$–6 s and a later, steep decline, beginning roughly at $t \approx 15$ s.

(iii) SFHx (green lines) is similar to SFHo, displaying a peak of tL_ν at a slightly earlier time and with a final decrease that is slightly delayed compared to SFHo.

(iv) LS220 (red lines) leads to a peak in tL_ν at $t \approx 2$ s and shows a more shallow decline afterward, forming a plateaulike shape in the time interval $2s \lesssim t \lesssim 10$ s (i.e., L_ν follows approximately $L_\nu \propto t^{-1}$) before a steeper decline sets in at $t \gtrsim 15$ s.

In simulations without muons (see the right panels in Fig. 12 and the data block at the bottom of Tables II and III in Appendix A), the product of time and luminosity for all ν species starts to become exponentially suppressed already at $t < 10$ s, with DD2 (blue lines) leading to a faster cooling than SFHo (orange lines).

To explicitly demonstrate the impact of convection and muons by means of the $\bar{\nu}_e$ luminosity, Fig. 13 displays the time evolution of $tL_{\bar{\nu}_e}$ for the $1.62 M_\odot$ models including both convection and muons (blue lines) compared to the corresponding results without convection (orange) and without muons (green, if available) for the DD2 EOS (upper left panel), SFHo EOS (lower left panel), SFHx EOS (upper right panel), and LS220 EOS (lower right panel). For all the cases,

(i) the "absence of convection" leads to a considerable stretching of the PNS Kelvin-Helmholtz neutrino cooling time, with the most moderate change for DD2,

(ii) the "omission of muons" has a relatively mild effect on the evolution of the neutrino signals for the displayed $1.62 M_\odot$ models, making the suppression in the luminosity only slightly faster (because the NS becomes less compact with a lower binding energy), as visible by the green lines in the left panels.
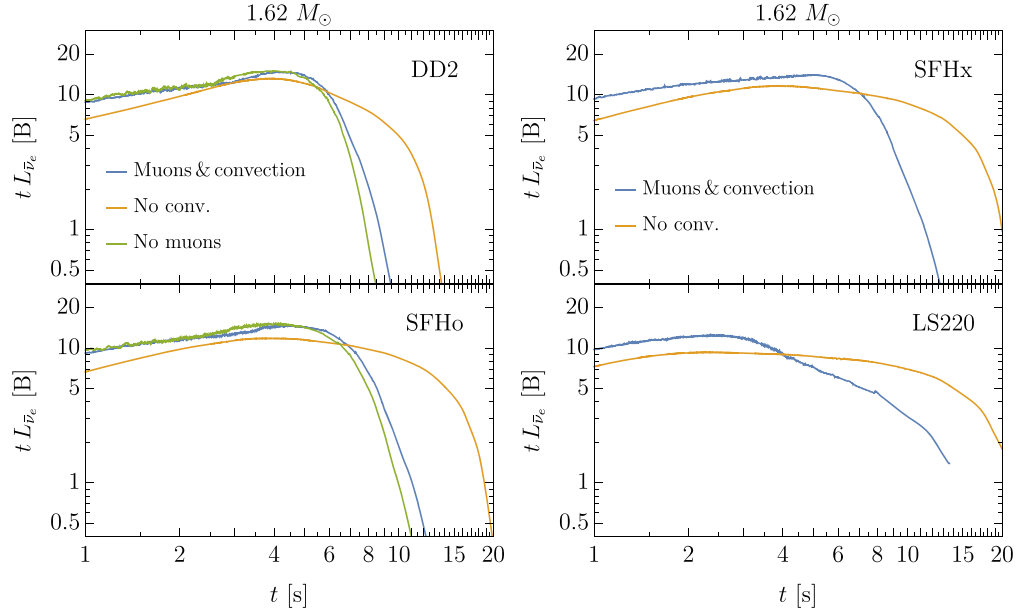
FIG. 13. Time evolution of the product of time and $\bar{\nu}_e$ luminosity, $tL_{\bar{\nu}_e}$, for $M_{\rm NS} = 1.62 M_\odot$ and different EOS, namely, DD2 and SFHo (left) and SFHx and LS220 (right), comparing models with both convection and muons (blue), without convection (orange), and without muons (green). Simulations using SFHx and LS220 without muons are not available.

To quantitatively assess the impact of these variations of the input physics of our models, we also fit the neutrino and antineutrino signals of the additional simulations with the expression of Eq. (2) and compare the best-fit parameters with those obtained in our benchmark simulations. As an example, Fig. 14 presents the simulation data (blue) and their best fits (orange) in the time interval of interest for $\bar{\nu}_e$ results from the simulations without convection (DD2 and SFHo in the top panels and SFHx and LS220 in the middle panels) and from our two simulations without muons (bottom panels). For the simulations without muons, where the neutrino signal does not experience major changes, the agreement between data and fits is similarly good as for our benchmark simulations. For the simulations without convection, the fit is still of excellent quality for DD2, although the omission of convection has altered the shape of the curve of $tL_{\bar{\nu}_e}$ (see Fig. 13). In contrast, we obtain visibly larger discrepancies between fits and data for the nonconvective simulations with SFHo and SFHx, for which, in particular, the shape of $tL_{\bar{\nu}_e}$ in the power-law dominated early phase cannot be reproduced as well as for models that include convection. Notably, the fits for $\bar{\nu}_e$ (and similarly for all other neutrino species) slightly overestimate tL_ν at $t \approx 1$ s and tend to peak only at somewhat later times. Finally, the plateaulike region of tL_ν in the simulation results for LS220 implies a best-fit value of $\alpha \approx 1$, with the luminosity fit overestimating the data at $t \approx 1$ s and following well a t^{-1} power law before being exponentially suppressed at $t \gtrsim 10$ s. Our findings

for all other neutrino species are analogous. In Tables X and XI in Appendix E, we provide the best-fit parameter values and their 1σ errors for electron and muon neutrinos and antineutrinos, for our $1.62 M_\odot$ models with different EOSs and varied input physics.

As further discussed in Appendix E, the parameters of nonconvective models adopt best-fit values that are well outside the 1σ confidence bands found for the benchmark simulations. This fact underlines the strong impact of convection on the neutrino signal. As general trends, we find in simulations with class A EOSs in the absence of convection that

(i) C decreases because of the lack of convective enhancement of the luminosities at early times,

(ii) τ becomes larger because of the extended PNS neutrino cooling time without convective energy transport, and

(iii) n becomes smaller to account for the considerable signal stretching at late times,

which implies that the exponential luminosity decline starts at later times and also proceeds more slowly. For $\bar{\nu}_e$ in model 1.62-DD2-c we notice an exception from the described general trends with respect to $\tau_{\bar{\nu}_e}$, which is slightly smaller than the value of the corresponding model with convection (see Table X and Fig. 16 in Appendix E). In this case, the mild decrease of $\tau_{\bar{\nu}_e}$ seems to be compensated by a reduction of $n_{\bar{\nu}_e}$ by a factor ~ 3 compared to the nonconvective model, which is by far the largest relative change for any neutrino species in all models with vs without convection. Interestingly, the change in α
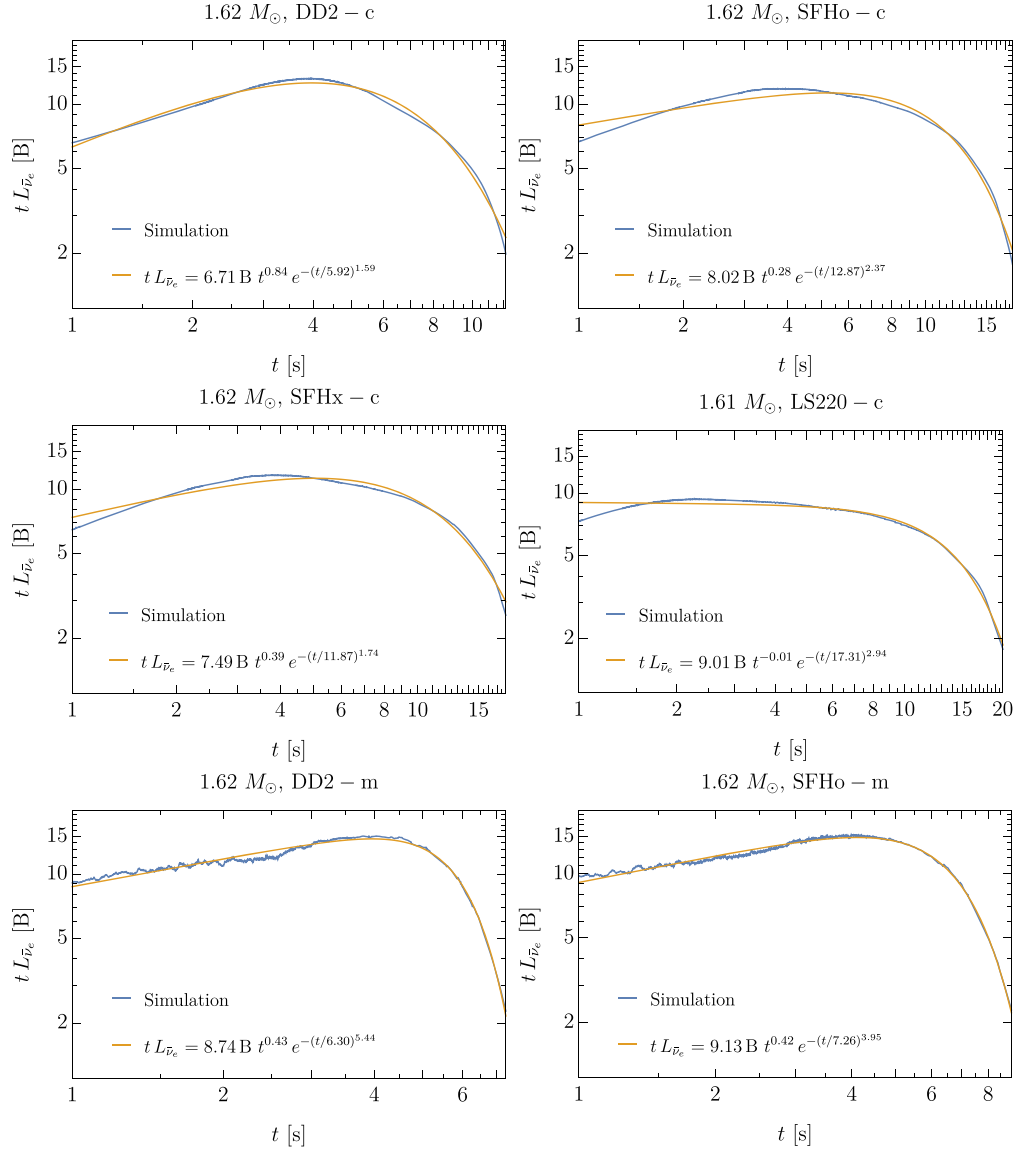
FIG. 14. Time evolution of the product of time and $\bar{\nu}_e$ luminosity, $tL_{\bar{\nu}_e}$, for simulation data (blue) and their fits (orange). The different panels show results for simulations without convection or without muons, namely, of models 1.62-DD2-c (top left), 1.62-SFHo-c (top right), 1.62-SFHx-c (middle left), 1.61-LS220-c (middle right), 1.62-DD2-m (bottom left), and 1.62-SFHo-m (bottom right). We consider data up to $t_{\bar{\nu}_e,c}$ for simulations with DD2 and SFHo and up to $t_{\bar{\nu}_e,Co}$ for 1-62-SFHx-c and 1.61-LS220-c (see Appendix A for more details).

depends on the EOS and neutrino species, showing, for instance, a decrease in 1.62-DD2-c compared to 1.62-DD2, an increase in 1.62-SFHo-c compared to 1.62-SFHo, and a decrease or slight increase in 1.62-SFHx-c compared to 1.62-SFHx depending on the type of neutrino. This nonuniform behavior points to differences in the influence of the EOS on PNS convection and the associated effects on the emission of different kinds of neutrinos during the early PNS cooling phase.

For simulations with the LS220 EOS, partly because of the poorer quality of the fits for the benchmark models, the omission of convection leads to radical changes in the values of the best-fit parameters. Indeed, LS220 simulations without convection show positive values of α (around unity), much larger values of τ and n compared to the full-physics cases, and values of C that are well compatible with those of simulations with the other EOSs including and excluding convection, i.e., the C values are close to the luminosity values at 1 s instead of being several 100 B/s for our benchmark models. Finally, the weaker impact of muons on the neutrino signal is highlighted by the small changes in the best-fit parameters obtained for simulations without muons, as further detailed in Appendix E.
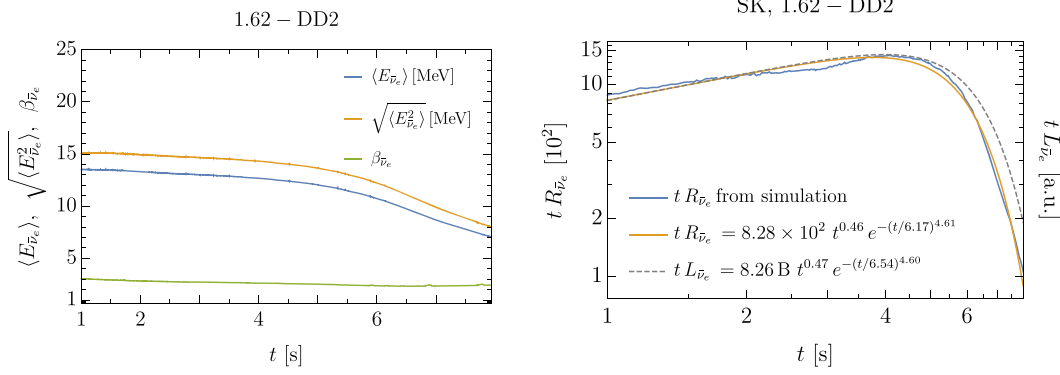
FIG. 15. Left: Simulation results for the average energy $\langle E_{\bar{\nu}_e} \rangle$ (blue), rms energy $\sqrt{\langle E_{\bar{\nu}_e}^2 \rangle}$ (orange), and spectral shape parameter $\beta_{\bar{\nu}_e}$ (green) from model 1.62-DD2. Right: $\bar{\nu}_e$-induced counting rate $tR_{\bar{\nu}_e}$ in SK computed from simulation data (blue), the fit of the counting rate (orange), and the fit of $tL_{\bar{\nu}_e}$ (dashed line).

VII. COUNTING RATE IN NEUTRINO DETECTORS

In order to exemplify a possible application of our luminosity fits, we discuss in this section the time evolution of the counting rate $tR_\nu(t)$ in a neutrino detector that will monitor the $tL_\nu(t)$ evolution in the case of a future Galactic SN explosion. We will demonstrate that our fitting recipe is also useful for fitting the observed neutrino signal. For this purpose, we consider as a reference case a SN at a distance of $D = 10$ kpc and evaluate the predicted signal in the water Cherenkov detector of Super-Kamiokande (SK) [55,56], inspired by the analysis in Ref. [57].

We consider the following ν differential flux per unit energy in MeV^{-1} s^{-1} cm^{-2}:

$$\mathcal{F}_\nu^0(E_\nu) = \frac{dF_\nu}{dE_\nu}$$
$$= \frac{L_\nu}{4\pi D^2 \langle E_\nu \rangle} \frac{(1+\beta_\nu)^{1+\beta_\nu}}{\Gamma(1+\beta_\nu)\langle E_\nu \rangle} \left(\frac{E_\nu}{\langle E_\nu \rangle}\right)^{\beta_\nu} e^{-(1+\beta_\nu)E_\nu/\langle E_\nu \rangle},$$

(5)

where the shape parameter β_ν is given by

$$\beta_\nu = \frac{\langle E_\nu^2 \rangle - 2\langle E_\nu \rangle^2}{\langle E_\nu \rangle^2 - \langle E_\nu^2 \rangle},$$

(6)

with $\langle E_\nu \rangle$ and $\langle E_\nu^2 \rangle$ being the average neutrino energy and the average squared neutrino energy, respectively.

In SK, the main detection process is inverse β decay, $\bar{\nu}_e p \to ne^+$, where the final-state positron shows up by its Cherenkov radiation. Because of the similarity of the electron and nonelectron antineutrino luminosities and spectra in our models during PNS Kelvin-Helmholtz cooling at times $t \gtrsim 1$ s after bounce, flavor conversions are not a major effect and can be neglected in our simplified analysis. Therefore, the expected rate can be written as

$$R_{\bar{\nu}_e} = N_p \int dE_e \int dE_\nu \mathcal{F}_{\bar{\nu}_e}(E_\nu)\sigma'(E_e, E_\nu), \quad (7)$$

where $N_p = 1.51 \times 10^{33}$ is the number of protons for a 22.5 kton Cherenkov detector. Here, we follow Ref. [58] for the limits of integration in dE_ν and we integrate the positron energies above the energy threshold $E_{\mathrm{th,SK}} = 5$ MeV. We mention that SK is essentially background-free. Estimates for the future Hyper-Kamiokande detector with fiducial mass of 187 kton [59] can be obtained by rescaling the counting rate computed for SK by a factor ~ 8.3, without affecting the temporal evolution of the signal.

To obtain a numerical estimate, we use data from model 1.62-DD2 as an example, but the same analysis is valid for all of the models. In the left panel of Fig. 15 we plot the average energy $\langle E_{\bar{\nu}_e} \rangle$, the root-mean-square (rms) energy $\sqrt{\langle E_{\bar{\nu}_e}^2 \rangle}$, and the shape parameter $\beta_{\bar{\nu}_e}$ as a function of the time, between 1 and $t_{\bar{\nu}_e,\mathrm{c}} = 7.94$ s. These quantities exhibit a weak time dependence, with $\langle E_{\bar{\nu}_e} \rangle \approx (12\text{–}13.5)$ MeV, $\sqrt{\langle E_{\bar{\nu}_e}^2 \rangle} \approx (14\text{–}15)$ MeV, and $\beta_{\bar{\nu}_e} \approx 2.5\text{–}3$ at $t \lesssim 5$ s and a decrease at later times. Here we focus on the 1.62-DD2 simulation as a representative case, but qualitatively similar results can be obtained with all the other models. Basic information on the time evolution of the mean neutrino energies for all considered EOSs can be found in Ref. [43] (see Fig. 3 therein, where the time evolution of the average neutrino energies for the $1.44M_\odot$ with different nuclear EOSs are shown).

The rate in SK can be simply estimated as

$$R_{\bar{\nu}_e} \approx \frac{L_{\bar{\nu}_e}}{4\pi D^2 \langle E_{\bar{\nu}_e} \rangle} N_{\mathrm{SK}} \langle \sigma \rangle, \quad (8)$$

where the average cross section is [57]

$$\langle \sigma \rangle = 7.37 \times 10^{-46} \text{ cm}^2 \frac{2+\beta_{\bar{\nu}_e}}{1+\beta_{\bar{\nu}_e}} \langle E_{\bar{\nu}_e} \rangle^{2.15} \times \left(\frac{76.64}{\beta_{\bar{\nu}_e}^{0.021}} - \frac{\langle E_{\bar{\nu}_e} \rangle}{\beta_{\bar{\nu}_e}^{0.24}}\right)$$
$$\times \left[1 - \exp\left(\frac{-0.25+0.55\langle E_{\bar{\nu}_e} \rangle}{2.2+\beta_{\bar{\nu}_e}} - \frac{1+1.6\beta_{\bar{\nu}_e}}{1+4\beta_{\bar{\nu}_e}}\langle E_{\bar{\nu}_e} \rangle\right)\right],$$

(9)

dependent on $\langle E_{\bar{\nu}_e}\rangle$ and $\beta_{\bar{\nu}_e}$ [and also on $\sqrt{\langle E_{\bar{\nu}_e}^2\rangle}$ via Eq. (6)]. Therefore, we expect that the observed rate $R_{\bar{\nu}_e}$ will follow the time dependence of the neutrino luminosity because of the weak time dependence of the other parameters, and that we can also fit it with our analytical formula in Eq. (2). In the right panel of Fig. 15, we show the quantity $tR_{\bar{\nu}_e}$ obtained from Eq. (7) using data from model 1.62-DD2 (blue line), its fit (orange), and the fitted $tL_{\bar{\nu}_e}$ (dashed line). As shown by the best-fit parameters for $tR_{\bar{\nu}_e}$ given in the plot, the fit leads to $C = 8.28 \times 10^2$ s^{-1}, $\alpha = 0.54$, $\tau = 6.17$ s, and $n = 4.61$, to be compared with the ones for $tL_{\bar{\nu}_e}$. The parameters $\alpha_{\bar{\nu}_e}$, $\tau_{\bar{\nu}_e}$, and $n_{\bar{\nu}_e}$ are well reconstructed, while one could get information on the normalization factor $C_{\bar{\nu}_e}$ by inverting Eq. (8). The slight difference between the parameters α, τ, and n reconstructed from the rate and the original ones for $L_{\bar{\nu}_e}$ can be explained by the weak time dependence of $\langle E_{\nu}\rangle$, $\langle E_{\nu}^2\rangle$, and β_{ν} entering in the computation of the rate. Therefore, one can fit the detected event rate with the same functional form used for the luminosity, and from the reconstructed fitting parameters one can get information on the PNS mass and on the EOS, as discussed in the previous sections. However, the accurate reconstruction of the parameters is beyond the scope of this analysis and will be the subject of future work dealing with their possible reconstruction using current and future neutrino detectors. There, more comprehensive information on the time evolution of $\langle E_{\nu}\rangle$, $\langle E_{\nu}^2\rangle$, and β_{ν} will be provided.

VIII. CONCLUSIONS

In this paper, we have investigated whether the simple analytical function of Eq. (2) can be used as a parametric fit to the SN neutrino luminosities during the Kelvin-Helmholtz cooling phase of the PNS. For this purpose, we have considered a set of several 1D simulations for different NS masses and EOSs. Our benchmark models account for PNS convection, which has a strong impact on the cooling evolution and its associated neutrino signal. In particular, we presented fits for the time-dependent neutrino luminosities from numerical PNS cooling simulations and reported systematic dependences of the fitting-parameter values as functions of the NS mass. Future work is desirable where these fits are connected to analytic descriptions and basic PNS and EOS properties in a more formal way, e.g., similar to what was done for PNS cooling models that did not include the effects of PNS convection (see, e.g., [41,60]).

Our fit function employs four free parameters, namely, a normalization factor C, a power-law exponent α for the time, an exponential cooling timescale τ, and an exponent n of (t/τ) in the exponential function. Their characteristic dependence on the PNS mass and on the EOS can be used to draw inferences on these latter properties, if the parameters are deduced from the neutrino signal of a future Galactic SN explosion. For this purpose, we plan to

investigate in future work how one can infer the parameter values of the neutrino luminosity from the SN neutrino signal measured in large underground detectors. We have demonstrated that this possibility is facilitated by the fact that the time evolution of the detected event rate depends on the neutrino luminosity L_{ν}, the average neutrino energy $\langle E_{\nu}\rangle$, and the rms energy $\sqrt{\langle E_{\nu}^2\rangle}$, but the time dependence of $\langle E_{\nu}\rangle$ and $\sqrt{\langle E_{\nu}^2\rangle}$ is weak. This allowed us to show that Eq. (2) provides a good functional form to also fit the time evolution of the observed neutrino signal. Therefore, for a first estimation of the L_{ν}-fit parameters from the event rate measured by a SN neutrino detector, one can simply apply our analytical expression for the luminosity fit and make use of the assumption that the average neutrino energy and the pinching parameter characterizing the spectral shape are constant in time.

A number of caveats of our study reported here need to be mentioned. First, the present analysis and our proposed luminosity fit are based on 1D SN and PNS cooling simulations using a fairly limited set of cases for the NS EOS. The general applicability of the fit function of Eq. (2) needs confirmation by testing a much larger variety of EOS models with a wide range of fundamental nuclear physics inputs that are compatible with all experimental, theoretical, and astrophysical constraints on the properties of nuclear matter and observed NSs. In particular, possible correlations of some of the fitting parameters [e.g., the relation in Eq. (4)] require confirmation based on a wider spectrum of nuclear EOS representations. Second, our 1D SN and PNS calculations disregard 3D effects such as long-lasting accretion onto the PNS (continuing also after the onset of the explosion, when in 1D models accretion abruptly stops) and fallback of some initial explosion ejecta during the late PNS evolution [43,61,62]. Moreover, the mixing-length treatment of PNS convection in our 1D models will have to be validated by long-time 3D simulations of PNS cooling once such calculations with good spatial resolution become available. In particular, this will also provide a test whether the fit function of Eq. (2) and our best-fit parameter values are compatible with 3D results for PNS cooling. If so, any deviation from the luminosity evolution described by our fit function would signal additional contributions to the neutrino emission added on top of the cooling component from the PNS. Thus, our L_{ν} fit could help to diagnose, disentangle, and describe such secondary neutrino emission phenomena in the neutrino measurement for a future Galactic SN. Finally, it will have to be seen how our fitting function reacts to additional, so far disregarded effects of potential importance in neutrino cooling SN cores, for example, fast flavor conversion of neutrino-antineutrino pairs, which could have a major impact on the neutrino emission properties [63,64], or extra cooling associated with the emission of light, weakly interacting beyond-standard-model particles (e.g., axions [65]). Again, our neutrino luminosity fits could help to diagnose such effects beyond

current standard SN modeling, once simulations including this new physics become available to be analyzed for long-time fitting.

In conclusion, we are confident that the simplicity of our fitting procedure will make it a useful tool for the neutrino community to describe the SN neutrino signal expected in a high-statistics detection, to probe a future SN neutrino measurement, and to infer valuable information on the PNS mass, nuclear EOS, and different signal components (see Ref. [66] for a recent approach in this direction).

The considered model results are adopted from Ref. [43] and are available in the Garching Core-collapse Supernova Archive [49] upon request.

APPENDIX A: TABLES FOR THE FINAL-TIME PARAMETERS

Here we provide the values of the final simulation time $t_{\rm fin}$, the time $t_{\nu_i,\max}$ when the quantity tL_{ν_i} reaches its maximum, $t_{\nu_i,\max}L_{\nu_i}(t_{\nu_i,\max}) \equiv t_{\nu_i,\max}L_{\nu_i,\max}$, and the selected cut time $t_{\nu_i,c}$, for neutrinos in Table II and for antineutrinos in Table III for all the simulations considered in our study. For each (anti)neutrino species, the selected cut time $t_{\nu_i,c}$ is the time when the quantity tL_{ν_i} is

TABLE II.   Times $t_{\nu_i,\max}$ when tL_{ν_i} adopts its maximum $t_{\nu_i,\max}L_{\nu_i,\max}$ and times $t_{\nu_i,c}$ when $X^c_{\nu_i} = 0.15$ for all neutrino species ν_i. Bold print marks values corresponding to $t_{\nu_i,c} > t_{\rm fin}$, i.e., cases when the simulation was stopped before $t_{\nu_i,c}$ was reached.

Model	$t_{\rm fin}$ (s)	$t_{\nu_e,\max}$ (s)	$t_{\nu_e,c}$ (s)	$t_{\nu_\mu,\max}$ (s)	$t_{\nu_\mu,c}$ (s)	$t_{\nu_\tau,\max}$ (s)	$t_{\nu_\tau,c}$ (s)
1.36-DD2	8.69	3.14	6.99	4.03	6.98	3.81	7.01
1.36-SFHo	10.50	3.09	8.51	4.00	8.65	4.11	8.62
1.36-SFHx	10.06	3.62	8.69	4.25	8.91	4.18	8.86
1.36-LS220	12.36	1.81	10.72	1.94	10.52	1.99	10.44
1.44-DD2	13.72	3.13	7.33	4.14	7.34	4.05	7.38
1.44-SFHo	15.00	3.27	8.96	4.24	9.10	4.18	9.09
1.44-SFHx	11.72	3.71	9.13	3.78	9.36	4.19	9.32
1.44-LS220	14.84	2.14	11.33	1.99	11.14	2.14	11.09
1.62-DD2	10.75	3.94	8.02	4.26	8.06	4.52	8.12
1.62-SFHo	14.26	3.46	9.89	4.71	10.06	4.73	10.06
1.62-SFHx	13.45	4.28	10.09	4.27	10.36	4.98	10.36
1.62-LS220	13.58	2.35	12.75	2.43	12.55	2.44	12.52
1.77-DD2	11.26	4.65	8.61	4.99	8.66	4.65	8.74
1.77-SFHo	13.28	4.98	10.65	4.98	10.85	4.98	10.84
1.77-SFHx	13.91	4.81	10.92	5.40	11.21	5.40	11.19
1.77-LS220	16.33	2.51	13.83	2.51	13.69	2.63	13.68
1.93-DD2	12.81	5.03	9.23	5.52	9.32	5.03	9.39
1.93-SFHo	15.52	5.37	11.55	5.26	11.79	5.47	11.82
1.93-SFHx	16.38	5.54	11.86	5.54	12.19	6.00	12.26
1.93-LS220	19.95	2.87	14.79	3.16	14.69	3.02	14.90
1.62-DD2-c	13.95	4.15	12.47	4.33	12.54	4.24	12.54
1.62-SFHo-c	19.74	4.38	18.02	5.20	18.18	4.89	18.05
1.62-SFHx-c	18.75	4.22	**> 18.75**	4.74	**> 18.75**	4.75	**> 18.75**
1.61-LS220-c	20.92	4.06	**> 20.92**	2.51	**> 20.92**	2.53	**> 20.92**
1.62-DD2-m	9.58	3.90	7.38	3.90	7.46	3.90	7.46
1.62-SFHo-m	13.55	3.95	9.15	4.47	9.38	4.47	9.38

TABLE III.   Times $t_{\bar{\nu}_i,\mathrm{max}}$ when $tL_{\bar{\nu}_i}$ adopts its maximum $t_{\bar{\nu}_i,\mathrm{max}}L_{\bar{\nu}_i,\mathrm{max}}$ and times $t_{\bar{\nu}_i,\mathrm{c}}$ when $X^c_{\bar{\nu}_i} = 0.15$ for all antineutrino species $\bar{\nu}_i$. Bold print marks values corresponding to $t_{\bar{\nu}_i,c} > t_{\mathrm{fin}}$, i.e., cases when the simulation was stopped before $t_{\bar{\nu}_i,c}$ was reached.

Model	t_{fin} (s)	$t_{\bar{\nu}_e,\mathrm{max}}$ (s)	$t_{\bar{\nu}_e,\mathrm{c}}$ (s)	$t_{\bar{\nu}_\mu,\mathrm{max}}$ (s)	$t_{\bar{\nu}_\mu,\mathrm{c}}$ (s)	$t_{\bar{\nu}_\tau,\mathrm{max}}$ (s)	$t_{\bar{\nu}_\tau,\mathrm{c}}$ (s)
1.36-DD2	8.69	3.56	6.89	3.31	7.01	3.81	7.00
1.36-SFHo	10.50	4.08	8.40	4.07	8.68	4.10	8.61
1.36-SFHx	10.06	4.12	8.65	3.77	8.94	4.18	8.84
1.36-LS220	12.36	1.96	10.45	1.95	10.31	1.99	10.39
1.44-DD2	13.72	3.87	7.22	3.83	7.37	4.05	7.37
1.44-SFHo	15.00	4.47	8.20	4.47	9.11	4.18	9.07
1.44-SFHx	11.72	4.19	9.08	4.08	9.40	4.19	9.30
1.44-LS220	14.84	1.93	11.08	1.93	10.95	2.14	11.03
1.62-DD2	10.75	4.12	7.94	4.06	8.11	4.52	8.10
1.62-SFHo	14.26	4.39	9.74	3.73	10.09	4.72	10.04
1.62-SFHx	13.45	5.00	10.06	4.36	10.46	4.88	10.34
1.62-LS220	13.58	2.36	12.44	2.35	12.23	2.36	12.43
1.77-DD2	11.26	4.45	8.51	4.49	8.72	4.65	8.72
1.77-SFHo	13.28	4.98	10.50	4.50	10.88	4.98	10.82
1.77-SFHx	13.91	5.40	10.89	5.17	11.28	5.40	11.17
1.77-LS220	16.33	2.67	13.56	2.67	13.24	2.63	13.55
1.93-DD2	12.81	5.03	9.11	4.97	9.35	5.03	9.37
1.93-SFHo	15.52	5.47	11.38	5.50	11.83	5.47	11.80
1.93-SFHx	16.38	6.04	11.93	5.97	12.35	6.00	12.23
1.93-LS220	19.95	2.74	14.85	2.74	14.38	3.02	14.76
1.62-DD2-c	13.95	3.90	12.14	4.18	12.49	4.24	12.52
1.62-SFHo-c	19.74	4.32	17.82	4.49	18.12	4.49	18.12
1.62-SFHx-c	18.75	3.79	**> 18.75**	4.55	**> 18.75**	4.88	**> 18.75**
1.61-LS220-c	20.92	2.26	20.85	2.42	**> 20.92**	2.36	**> 20.92**
1.62-DD2-m	9.58	3.90	7.32	3.90	7.45	3.90	7.45
1.62-SFHo-m	13.55	4.13	9.00	4.47	9.37	4.47	9.37

TABLE IV.   The time $t_{\nu_i,\mathrm{max}}$ when tL_{ν_i} is maximum and the time $t_{\nu_i,\mathrm{Co}}$ for ν_e, $\bar{\nu}_e$, ν_μ, and $\bar{\nu}_\mu$ adopted to test the impact of convection in simulations where $X^{\mathrm{fin}}_{\nu_i} > 0.15$. For simulations with the SFHx EOS, $t_{\nu_i,\mathrm{Co}}$ is the time when $X^{\mathrm{Co}}_{\nu_i} = 0.22$, while for LS220 is the time when $X^{\mathrm{Co}}_{\nu_i} = 0.19$.

Model	t_{fin} (s)	$t_{\nu_e,\mathrm{max}}$ (s)	$t_{\nu_e,\mathrm{Co}}$ (s)	$t_{\bar{\nu}_e,\mathrm{max}}$ (s)	$t_{\bar{\nu}_e,\mathrm{Co}}$ (s)	$t_{\nu_\mu,\mathrm{max}}$ (s)	$t_{\nu_\mu,\mathrm{Co}}$ (s)	$t_{\bar{\nu}_\mu,\mathrm{max}}$ (s)	$t_{\bar{\nu}_\mu,\mathrm{Co}}$ (s)
1.62-SFHx	13.45	4.26	9.39	5.00	9.38	4.27	9.74	4.36	9.86
1.62-SFHx-c	18.75	4.22	18.09	3.79	17.99	4.74	18.73	4.55	18.64
1.62-LS220	13.58	2.35	11.92	2.36	11.58	2.43	11.68	2.35	10.98
1.61-LS220-c	20.92	4.06	20.62	2.26	20.03	2.51	20.81	2.42	20.49

reduced relative to its maximum value by a factor $X^c_{\nu_i} \equiv t_{\nu_i,c}L_{\nu_i,c}/t_{\nu_i,\mathrm{max}}L_{\nu_i,\mathrm{max}} = 0.15$, in order to take a common final time for all neutrino species. As shown by the quantities in bold print in Tables II and III, $t_{\nu_i,c} > t_{\mathrm{fin}}$ for 1.62-SFHx-c and 1.61-LS220-c, i.e., these simulations stop before reaching $t_{\nu_i,c}$. Therefore, to check the impact of convection in these two cases, we cut our simulation outputs at earlier times, $t_{\nu_i,\mathrm{Co}}$, when $X^{\mathrm{Co}}_{\nu_i} = t_{\nu_i,\mathrm{Co}}L_{\nu_i,\mathrm{Co}}/t_{\nu_i,\mathrm{max}}L_{\nu_i,\mathrm{max}} = 0.22$ for simulations with SFHx and $X^{\mathrm{Co}}_{\nu_i} = 0.19$ for LS220. We show t_{fin}, $t_{\nu_i,\mathrm{max}}$, and $t_{\nu_i,\mathrm{Co}}$ used to check the impact of convection for electron and muon (anti)neutrinos in Table IV.

APPENDIX B: TABLES FOR BEST-FIT PARAMETERS OF LUMINOSITIES FOR NEUTRINOS AND ANTINEUTRINOS OF ALL FLAVORS

Here we report the best-fit values with 1σ errors of the parameters characterizing the fit for the time evolution of all neutrino and antineutrino luminosities in the time interval from $1s$ to $t_{\nu_i,c}$ (see Appendix A for more details). The fit function is given by Eq. (2),

$$L_{\nu_i}(t) = Ct^{-\alpha}e^{-(t/\tau)^n},$$

TABLE V. Best-fit parameters with 1σ errors for $L_{\nu_i} = Ct^{-\alpha}e^{-(t/\tau)^n}$ in the time interval between 1 s and $t_{\nu_i,c}$ for ν_e (left) and $\bar{\nu}_e$ (right) for our benchmark models.

Model	C_{ν_e} (B/s)	α_{ν_e}	τ_{ν_e} (s)	n_{ν_e}	$C_{\bar{\nu}_e}$ (B/s)	$\alpha_{\bar{\nu}_e}$	$\tau_{\bar{\nu}_e}$ (s)	$n_{\bar{\nu}_e}$
1.36-DD2	5.485 ± 0.007	0.410 ± 0.002	5.384 ± 0.004	3.660 ± 0.008	6.322 ± 0.010	0.550 ± 0.002	5.659 ± 0.004	4.462 ± 0.012
1.36-SFHo	6.339 ± 0.004	0.604 ± 0.001	6.573 ± 0.002	3.435 ± 0.003	6.730 ± 0.008	0.644 ± 0.001	6.756 ± 0.004	3.948 ± 0.007
1.36-SFHx	6.345 ± 0.004	0.626 ± 0.001	6.720 ± 0.003	3.431 ± 0.004	6.973 ± 0.007	0.686 ± 0.001	6.933 ± 0.003	3.881 ± 0.006
1.36-LS220	9.784 ± 0.063	0.727 ± 0.010	4.410 ± 0.089	1.061 ± 0.011	10.63 ± 0.08	0.795 ± 0.012	4.471 ± 0.106	1.052 ± 0.013
1.44-DD2	6.050 ± 0.008	0.428 ± 0.002	5.724 ± 0.004	3.835 ± 0.008	6.996 ± 0.011	0.543 ± 0.002	5.964 ± 0.004	4.582 ± 0.011
1.44-SFHo	7.054 ± 0.004	0.606 ± 0.001	6.953 ± 0.002	3.502 ± 0.003	7.515 ± 0.007	0.627 ± 0.001	7.077 ± 0.003	3.928 ± 0.006
1.44-SFHx	7.085 ± 0.004	0.637 ± 0.001	7.148 ± 0.002	3.547 ± 0.003	7.818 ± 0.007	0.680 ± 0.001	7.301 ± 0.003	3.916 ± 0.006
1.44-LS220	120.3 ± 18.1	−0.504 ± 0.048	0.113 ± 0.020	0.449 ± 0.010	112.7 ± 15.6	−0.430 ± 0.046	0.135 ± 0.022	0.460 ± 0.010
1.62-DD2	7.040 ± 0.010	0.430 ± 0.002	6.319 ± 0.004	3.959 ± 0.008	8.260 ± 0.014	0.529 ± 0.002	6.538 ± 0.004	4.599 ± 0.012
1.62-SFHo	8.308 ± 0.005	0.601 ± 0.001	7.743 ± 0.002	3.639 ± 0.003	8.967 ± 0.008	0.612 ± 0.001	7.823 ± 0.003	3.971 ± 0.005
1.62-SFHx	8.317 ± 0.006	0.618 ± 0.001	7.923 ± 0.003	3.647 ± 0.004	9.474 ± 0.009	0.672 ± 0.001	8.091 ± 0.003	3.979 ± 0.005
1.62-LS220	266.7 ± 50.4	−0.672 ± 0.053	0.052 ± 0.011	0.404 ± 0.009	253.5 ± 37.3	−0.670 ± 0.043	0.063 ± 0.010	0.417 ± 0.007
1.77-DD2	7.948 ± 0.010	0.448 ± 0.001	6.875 ± 0.004	4.201 ± 0.008	9.428 ± 0.014	0.534 ± 0.002	7.068 ± 0.004	4.755 ± 0.011
1.77-SFHo	9.306 ± 0.006	0.585 ± 0.001	8.372 ± 0.002	3.718 ± 0.003	10.21 ± 0.01	0.599 ± 0.001	8.443 ± 0.003	4.000 ± 0.004
1.77-SFHx	9.346 ± 0.005	0.604 ± 0.001	8.594 ± 0.002	3.678 ± 0.003	10.92 ± 0.01	0.669 ± 0.001	8.795 ± 0.003	4.021 ± 0.005
1.77-LS220	404.1 ± 100.0	−0.745 ± 0.066	0.037 ± 0.010	0.384 ± 0.010	359.8 ± 60.9	−0.755 ± 0.048	0.048 ± 0.009	0.401 ± 0.008
1.93-DD2	8.865 ± 0.013	0.445 ± 0.002	7.419 ± 0.004	4.349 ± 0.008	10.73 ± 0.02	0.534 ± 0.001	7.625 ± 0.003	4.941 ± 0.010
1.93-SFHo	10.474 ± 0.007	0.575 ± 0.001	9.072 ± 0.003	3.749 ± 0.004	11.45 ± 0.01	0.577 ± 0.001	9.129 ± 0.003	4.016 ± 0.004
1.93-SFHx	10.664 ± 0.005	0.6170 ± 0.0005	9.542 ± 0.002	3.971 ± 0.003	12.48 ± 0.01	0.666 ± 0.001	9.681 ± 0.003	4.163 ± 0.004
1.93-LS220	608.1 ± 171.7	−0.882 ± 0.073	0.026 ± 0.008	0.371 ± 0.010	477.1 ± 85.8	−0.872 ± 0.050	0.039 ± 0.008	0.392 ± 0.008

TABLE VI. Best-fit parameters with 1σ errors for $L_{\nu_i} = C t^{-\alpha} e^{-(t/\tau)^n}$ in the time interval between 1 s and $t_{\nu_i,c}$ for ν_μ (left) and $\bar{\nu}_\mu$ (right) for our benchmark models.

Model	C_{ν_μ} (B/s)	α_{ν_μ}	τ_{ν_μ} (s)	n_{ν_μ}	$C_{\bar{\nu}_\mu}$ (B/s)	$\alpha_{\bar{\nu}_\mu}$	$\tau_{\bar{\nu}_\mu}$ (s)	$n_{\bar{\nu}_\mu}$
1.36-DD2	6.333 ± 0.008	0.421 ± 0.002	5.687 ± 0.003	4.413 ± 0.009	6.927 ± 0.008	0.479 ± 0.002	5.754 ± 0.003	4.468 ± 0.008
1.36-SFHo	7.053 ± 0.006	0.579 ± 0.001	6.945 ± 0.003	3.926 ± 0.005	7.679 ± 0.004	0.634 ± 0.001	7.067 ± 0.002	4.045 ± 0.003
1.36-SFHx	7.113 ± 0.007	0.598 ± 0.001	7.110 ± 0.003	3.873 ± 0.005	7.868 ± 0.004	0.662 ± 0.001	7.245 ± 0.002	3.964 ± 0.003
1.36-LS220	69.88 ± 8.62	-0.177 ± 0.045	0.252 ± 0.040	0.499 ± 0.012	107.4 ± 17.9	-0.301 ± 0.057	0.164 ± 0.033	0.473 ± 0.013
1.44-DD2	7.036 ± 0.009	0.426 ± 0.002	5.999 ± 0.003	4.501 ± 0.009	7.740 ± 0.008	0.489 ± 0.001	6.084 ± 0.002	4.607 ± 0.008
1.44-SFHo	7.951 ± 0.006	0.581 ± 0.001	7.317 ± 0.003	3.953 ± 0.005	8.662 ± 0.004	0.631 ± 0.001	7.429 ± 0.002	4.025 ± 0.003
1.44-SFHx	8.053 ± 0.007	0.611 ± 0.001	7.535 ± 0.003	3.998 ± 0.005	8.940 ± 0.004	0.674 ± 0.001	7.671 ± 0.001	4.053 ± 0.003
1.44-LS220	234.9 ± 47.5	-0.514 ± 0.058	0.068 ± 0.016	0.418 ± 0.011	297.6 ± 66.0	-0.573 ± 0.063	0.059 ± 0.014	0.416 ± 0.011
1.62-DD2	8.428 ± 0.011	0.430 ± 0.002	6.595 ± 0.003	4.542 ± 0.009	9.271 ± 0.012	0.486 ± 0.001	6.676 ± 0.003	4.569 ± 0.009
1.62-SFHo	9.669 ± 0.008	0.582 ± 0.001	8.104 ± 0.003	4.022 ± 0.005	10.60 ± 0.01	0.633 ± 0.001	8.239 ± 0.002	4.094 ± 0.003
1.62-SFHx	9.802 ± 0.009	0.603 ± 0.001	8.318 ± 0.003	3.961 ± 0.005	10.98 ± 0.01	0.666 ± 0.001	8.466 ± 0.002	3.989 ± 0.004
1.62-LS220	430.2 ± 102.3	-0.612 ± 0.063	0.041 ± 0.011	0.388 ± 0.010	519.6 ± 128.6	-0.720 ± 0.067	0.039 ± 0.010	0.394 ± 0.011
1.77-DD2	9.685 ± 0.013	0.441 ± 0.001	7.120 ± 0.003	4.668 ± 0.009	10.72 ± 0.01	0.498 ± 0.001	7.217 ± 0.003	4.709 ± 0.008
1.77-SFHo	11.12 ± 0.01	0.574 ± 0.001	8.741 ± 0.002	4.045 ± 0.004	12.32 ± 0.01	0.6294 ± 0.0004	8.897 ± 0.001	4.105 ± 0.003
1.77-SFHx	11.43 ± 0.01	0.610 ± 0.001	9.052 ± 0.003	4.049 ± 0.005	12.92 ± 0.01	0.6769 ± 0.0005	9.236 ± 0.002	4.115 ± 0.003
1.77-LS220	531.9 ± 144.0	-0.634 ± 0.071	0.036 ± 0.011	0.380 ± 0.011	859.4 ± 272.3	-0.832 ± 0.081	0.026 ± 0.008	0.376 ± 0.012
1.93-DD2	11.00 ± 0.02	0.437 ± 0.002	7.650 ± 0.004	4.702 ± 0.010	12.47 ± 0.01	0.515 ± 0.001	7.802 ± 0.003	4.918 ± 0.008
1.93-SFHo	12.76 ± 0.01	0.563 ± 0.001	9.431 ± 0.003	3.968 ± 0.004	14.25 ± 0.01	0.6202 ± 0.0005	9.619 ± 0.002	4.049 ± 0.003
1.93-SFHx	13.38 ± 0.01	0.623 ± 0.001	9.976 ± 0.003	4.256 ± 0.004	15.11 ± 0.01	0.6803 ± 0.0004	10.148 ± 0.002	4.213 ± 0.003
1.93-LS220	785.6 ± 237.0	-0.767 ± 0.077	0.027 ± 0.009	0.370 ± 0.011	803.2 ± 240.7	-0.882 ± 0.081	0.032 ± 0.010	0.385 ± 0.012

TABLE VII. Best-fit parameters with 1σ errors for $L_{\nu_i} = Ct^{-\alpha}e^{-(t/\tau)^n}$ in the time interval between 1 s and $t_{\nu_i,c}$ for ν_τ (left) and $\bar{\nu}_\tau$ (right) for our benchmark models.

Model	C_{ν_τ} (B/s)	α_{ν_τ}	τ_{ν_τ} (s)	n_{ν_τ}	$C_{\bar{\nu}_\tau}$ (B/s)	$\alpha_{\bar{\nu}_\tau}$	$\tau_{\bar{\nu}_\tau}$ (s)	$n_{\bar{\nu}_\tau}$
1.36-DD2	6.433 ± 0.007	0.440 ± 0.001	5.730 ± 0.002	4.470 ± 0.007	6.701 ± 0.007	0.446 ± 0.001	5.726 ± 0.002	4.489 ± 0.007
1.36-SFHo	7.155 ± 0.003	0.603 ± 0.001	7.023 ± 0.001	4.116 ± 0.003	7.465 ± 0.003	0.609 ± 0.001	7.019 ± 0.001	4.129 ± 0.003
1.36-SFHx	7.272 ± 0.004	0.626 ± 0.001	7.196 ± 0.002	4.059 ± 0.003	7.584 ± 0.004	0.632 ± 0.001	7.190 ± 0.002	4.069 ± 0.003
1.36-LS220	87.76 ± 12.74	-0.285 ± 0.051	0.192 ± 0.034	0.483 ± 0.012	113.7 ± 19.1	-0.324 ± 0.056	0.148 ± 0.030	0.465 ± 0.012
1.44-DD2	7.137 ± 0.008	0.443 ± 0.001	6.043 ± 0.002	4.532 ± 0.007	7.442 ± 0.008	0.449 ± 0.001	6.040 ± 0.002	4.557 ± 0.007
1.44-SFHo	8.028 ± 0.003	0.5967 ± 0.0005	7.381 ± 0.001	4.089 ± 0.003	8.383 ± 0.003	0.6032 ± 0.0005	7.378 ± 0.001	4.104 ± 0.003
1.44-SFHx	8.210 ± 0.004	0.6346 ± 0.0005	7.612 ± 0.001	4.145 ± 0.003	8.570 ± 0.004	0.6403 ± 0.0005	7.606 ± 0.001	4.159 ± 0.003
1.44-LS220	397.3 ± 97.3	-0.696 ± 0.066	0.040 ± 0.010	0.397 ± 0.011	192.1 ± 36.2	-0.444 ± 0.057	0.093 ± 0.020	0.435 ± 0.011
1.62-DD2	8.499 ± 0.010	0.439 ± 0.001	6.634 ± 0.003	4.513 ± 0.008	8.878 ± 0.011	0.447 ± 0.001	6.633 ± 0.003	4.543 ± 0.008
1.62-SFHo	9.714 ± 0.005	0.5922 ± 0.0005	8.169 ± 0.001	4.121 ± 0.003	10.166 ± 0.005	0.5993 ± 0.0005	8.167 ± 0.001	4.141 ± 0.003
1.62-SFHx	9.953 ± 0.006	0.620 ± 0.001	8.395 ± 0.002	4.064 ± 0.004	10.41 ± 0.01	0.626 ± 0.001	8.389 ± 0.002	4.078 ± 0.004
1.62-LS220	366.1 ± 80.8	-0.623 ± 0.061	0.050 ± 0.012	0.401 ± 0.010	947.6 ± 293.1	-0.839 ± 0.075	0.019 ± 0.006	0.365 ± 0.011
1.77-DD2	9.731 ± 0.011	0.445 ± 0.001	7.157 ± 0.003	4.588 ± 0.008	10.18 ± 0.01	0.453 ± 0.001	7.158 ± 0.003	4.627 ± 0.008
1.77-SFHo	11.146 ± 0.005	0.5816 ± 0.0004	8.809 ± 0.001	4.115 ± 0.003	11.69 ± 0.01	0.5893 ± 0.0004	8.809 ± 0.001	4.139 ± 0.003
1.77-SFHx	11.57 ± 0.01	0.624 ± 0.001	9.138 ± 0.002	4.147 ± 0.003	12.11 ± 0.01	0.630 ± 0.001	9.131 ± 0.002	4.162 ± 0.003
1.77-LS220	1283 ± 457	-0.914 ± 0.084	0.015 ± 0.005	0.353 ± 0.011	1323 ± 490	-0.892 ± 0.088	0.015 ± 0.006	0.353 ± 0.012
1.93-DD2	11.11 ± 0.01	0.448 ± 0.001	7.712 ± 0.003	4.680 ± 0.008	11.65 ± 0.01	0.457 ± 0.001	7.715 ± 0.003	4.729 ± 0.008
1.93-SFHo	12.73 ± 0.01	0.5668 ± 0.0005	9.512 ± 0.002	4.022 ± 0.003	13.38 ± 0.01	0.5751 ± 0.0005	9.513 ± 0.002	4.047 ± 0.003
1.93-SFHx	13.41 ± 0.01	0.6261 ± 0.0005	10.042 ± 0.002	4.262 ± 0.003	14.07 ± 0.01	0.6322 ± 0.0005	10.036 ± 0.002	4.283 ± 0.003
1.93-LS220	1818 ± 672	-1.029 ± 0.086	0.011 ± 0.004	0.345 ± 0.011	1245 ± 422	-0.912 ± 0.083	0.018 ± 0.006	0.359 ± 0.011

with C, α, τ, and n being free parameters. We show values of the fit parameters for ν_e and $\bar{\nu}_e$ in Table V, for ν_μ and $\bar{\nu}_\mu$ in Table VI, and for ν_τ and $\bar{\nu}_\tau$ in Table VII, obtained with the NonlinearModelFit function in *Mathematica*.

APPENDIX C: TABLES FOR THE LINEAR RELATIONS BETWEEN LUMINOSITY-FITTING PARAMETERS AND PNS MASS

In Table VIII we provide the best-fit values and their 1σ errors for the parameters K_0 and K_1 that describe the linear dependencies of the parameter values in the L_ν fit of Eq. (2) on the PNS mass $M_{\rm NS}$ at fixed EOS, for all neutrino and antineutrino species,

$$K = K_0 + K_1 \frac{M_{\rm NS}}{M_\odot}, \qquad (\text{C1})$$

where $K = C$, α, τ, n. The larger values of the relative uncertainties on K_0 and K_1 in Table VIII and the widths of

the confidence bands in Figs. 8–10 suggest that the linear fits work better for class A EOSs than for LS220. At fixed EOS (in particular, for class A EOSs), the linear fits are excellent for C and τ and slightly worse for α and n, featuring larger relative errors of the best-fit values of the parameters in Eq. (C1) (see, e.g., the values of α_1 and n_1).

APPENDIX D: TABLES FOR PARAMETER VALUES OF THE CORRELATIONS BETWEEN τ AND α

We report in Table IX the best-fit values and the 1σ errors for the parameters A and B of the linear functions used for describing the correlations between τ (in seconds) and α [see Eq. (4)],

$$\tau(s) = A + B\alpha.$$

As shown in Table IX, the fit works better for neutrinos than for antineutrinos. Indeed, for $\bar{\nu}_e$ the error on the

TABLE VIII. Coefficients K_0 and K_1 with errors for the linear dependence on the PNS mass $K = K_0 + K_1 M_{\rm NS}/M_\odot$ at fixed EOS, for electron (upper data block), muon (central data block), and τ (lower data block) neutrinos and antineutrinos, obtained on grounds of simulation data in the time interval between 1 s and $t_{\nu_i,\rm c}$.

Neutrino	EOS	C_0 (B/s)	C_1 (B/s)	α_0	α_1	τ_0 (s)	τ_1 (s)	n_0	n_1
ν_e	DD2	-2.46 ± 0.14	5.87 ± 0.09	0.34 ± 0.03	0.06 ± 0.02	0.59 ± 0.09	3.54 ± 0.06	2.09 ± 0.15	1.17 ± 0.09
ν_e	SFHo	-3.29 ± 0.23	7.13 ± 0.14	0.68 ± 0.02	-0.05 ± 0.01	0.66 ± 0.06	4.36 ± 0.04	2.69 ± 0.12	0.57 ± 0.07
ν_e	SFHx	-3.66 ± 0.30	7.39 ± 0.18	0.68 ± 0.03	-0.04 ± 0.02	0.16 ± 0.29	4.82 ± 0.18	2.32 ± 0.25	0.82 ± 0.15
ν_e	LS220	-1347.9 ± 82.6	1003.5 ± 50.5	3.12 ± 1.66	-2.17 ± 1.01	9.64 ± 6.03	-5.36 ± 3.68	1.98 ± 0.85	-0.89 ± 0.52
$\bar{\nu}_e$	DD2	-4.07 ± 0.20	7.64 ± 0.12	0.58 ± 0.02	-0.03 ± 0.01	1.02 ± 0.06	3.42 ± 0.04	3.43 ± 0.20	0.76 ± 0.12
$\bar{\nu}_e$	SFHo	-4.40 ± 0.22	8.23 ± 0.13	0.79 ± 0.01	-0.11 ± 0.01	1.09 ± 0.04	4.16 ± 0.02	3.73 ± 0.05	0.15 ± 0.03
$\bar{\nu}_e$	SFHx	-6.05 ± 0.13	9.59 ± 0.08	0.73 ± 0.01	-0.035 ± 0.004	0.43 ± 0.22	4.76 ± 0.13	3.25 ± 0.11	0.46 ± 0.06
$\bar{\nu}_e$	LS220	-1050.0 ± 65.1	796.0 ± 39.7	3.37 ± 1.67	-2.31 ± 1.02	9.77 ± 6.08	-5.43 ± 3.72	1.92 ± 0.83	-0.85 ± 0.51
ν_μ	DD2	-4.72 ± 0.11	8.14 ± 0.07	0.38 ± 0.01	0.03 ± 0.01	1.05 ± 0.06	3.43 ± 0.04	3.75 ± 0.11	0.50 ± 0.07
ν_μ	SFHo	-6.37 ± 0.18	9.90 ± 0.11	0.62 ± 0.02	-0.03 ± 0.01	1.05 ± 0.05	4.35 ± 0.03	3.80 ± 0.17	0.11 ± 0.10
ν_μ	SFHx	-7.61 ± 0.43	10.82 ± 0.26	0.56 ± 0.02	0.03 ± 0.01	0.39 ± 0.25	4.93 ± 0.15	3.14 ± 0.26	0.55 ± 0.16
ν_μ	LS220	-1482.0 ± 155.4	1165.3 ± 94.9	0.82 ± 0.42	-0.84 ± 0.26	0.57 ± 0.26	-0.30 ± 0.16	0.72 ± 0.11	-0.19 ± 0.07
$\bar{\nu}_\mu$	DD2	-6.11 ± 0.42	9.56 ± 0.26	0.40 ± 0.02	0.05 ± 0.01	0.94 ± 0.08	3.55 ± 0.05	3.56 ± 0.27	0.67 ± 0.17
$\bar{\nu}_\mu$	SFHo	-7.85 ± 0.23	11.42 ± 0.14	0.66 ± 0.01	-0.02 ± 0.01	0.99 ± 0.02	4.47 ± 0.01	3.96 ± 0.13	0.06 ± 0.08
$\bar{\nu}_\mu$	SFHx	-9.22 ± 0.43	12.55 ± 0.26	0.63 ± 0.02	0.03 ± 0.01	0.41 ± 0.22	5.02 ± 0.14	3.46 ± 0.20	0.37 ± 0.12
$\bar{\nu}_\mu$	LS220	-1608.5 ± 407.4	1309.1 ± 248.8	0.85 ± 0.35	-0.93 ± 0.21	0.37 ± 0.15	-0.19 ± 0.09	0.64 ± 0.09	-0.14 ± 0.05
ν_τ	DD2	-4.60 ± 0.18	8.12 ± 0.11	0.42 ± 0.01	0.012 ± 0.005	1.05 ± 0.06	3.45 ± 0.03	4.04 ± 0.13	0.32 ± 0.08
ν_τ	SFHo	-5.99 ± 0.15	9.70 ± 0.09	0.68 ± 0.01	-0.06 ± 0.01	1.11 ± 0.02	4.36 ± 0.01	4.27 ± 0.13	-0.11 ± 0.08
ν_τ	SFHx	-7.17 ± 0.32	10.62 ± 0.19	0.64 ± 0.02	-0.009 ± 0.012	0.50 ± 0.23	4.91 ± 0.14	3.70 ± 0.22	0.27 ± 0.13
ν_τ	LS220	-4008.7 ± 943.6	2955.1 ± 576.3	1.09 ± 0.51	-1.11 ± 0.31	0.45 ± 0.20	-0.24 ± 0.12	0.73 ± 0.11	-0.21 ± 0.06
$\bar{\nu}_\tau$	DD2	-4.98 ± 0.20	8.59 ± 0.12	0.42 ± 0.01	0.017 ± 0.006	1.03 ± 0.06	3.46 ± 0.03	3.99 ± 0.13	0.37 ± 0.08
$\bar{\nu}_\tau$	SFHo	-6.49 ± 0.16	10.29 ± 0.10	0.69 ± 0.01	-0.06 ± 0.01	1.09 ± 0.02	4.37 ± 0.01	4.25 ± 0.14	-0.09 ± 0.08
$\bar{\nu}_\tau$	SFHx	-7.67 ± 0.35	11.22 ± 0.21	0.64 ± 0.02	-0.008 ± 0.012	0.50 ± 0.23	4.91 ± 0.14	3.69 ± 0.22	0.29 ± 0.13
$\bar{\nu}_\tau$	LS220	-2988.6 ± 809.8	2310.9 ± 494.6	1.09 ± 0.43	-1.09 ± 0.26	0.42 ± 0.12	-0.22 ± 0.07	0.71 ± 0.09	-0.20 ± 0.06

TABLE IX. Coefficients A and B with errors for the relation $\tau[s] = A + B\alpha$, for neutrinos (left) and antineutrinos (right), for all flavors and NS masses, obtained on grounds of simulation data in the time interval between 1 s and $t_{\nu_i,c}$.

Neutrino	M_{NS} ($M_\odot$)	A (s)	B (s)
ν_e	1.36	2.85 ± 0.03	6.17 ± 0.05
ν_e	1.44	2.80 ± 0.05	6.84 ± 0.09
ν_e	1.62	2.70 ± 0.08	8.42 ± 0.15
ν_e	1.77	1.95 ± 0.04	10.98 ± 0.08
ν_e	1.93	1.87 ± 0.17	12.47 ± 0.31
ν_μ	1.36	2.32 ± 0.04	8.00 ± 0.08
ν_μ	1.44	2.45 ± 0.11	8.34 ± 0.19
ν_μ	1.62	2.31 ± 0.02	9.96 ± 0.04
ν_μ	1.77	2.01 ± 0.32	11.63 ± 0.59
ν_μ	1.93	2.09 ± 0.64	12.80 ± 1.17
ν_τ	1.36	2.25 ± 0.04	7.91 ± 0.07
ν_τ	1.44	2.37 ± 0.24	8.32 ± 0.42
ν_τ	1.62	2.32 ± 0.14	9.83 ± 0.26
ν_τ	1.77	2.15 ± 0.46	11.30 ± 0.83
ν_τ	1.93	1.77 ± 0.84	13.38 ± 1.53

Neutrino	M_{NS} ($M_\odot$)	A (s)	B (s)
$\bar\nu_e$	1.36	0.33 ± 1.13	9.76 ± 1.79
$\bar\nu_e$	1.44	0.56 ± 1.53	10.08 ± 2.47
$\bar\nu_e$	1.62	0.79 ± 1.85	11.08 ± 3.04
$\bar\nu_e$	1.77	0.53 ± 2.82	12.61 ± 4.68
$\bar\nu_e$	1.93	0.40 ± 4.15	14.21 ± 6.98
$\bar\nu_\mu$	1.36	1.81 ± 0.16	8.24 ± 0.27
$\bar\nu_\mu$	1.44	1.78 ± 0.44	8.83 ± 0.73
$\bar\nu_\mu$	1.62	1.75 ± 0.32	10.16 ± 0.54
$\bar\nu_\mu$	1.77	1.46 ± 0.72	11.62 ± 1.19
$\bar\nu_\mu$	1.93	0.39 ± 1.34	14.53 ± 2.20
$\bar\nu_\tau$	1.36	2.20 ± 0.03	7.91 ± 0.06
$\bar\nu_\tau$	1.44	2.30 ± 0.23	8.34 ± 0.40
$\bar\nu_\tau$	1.62	2.22 ± 0.12	9.88 ± 0.22
$\bar\nu_\tau$	1.77	2.01 ± 0.43	11.41 ± 0.77
$\bar\nu_\tau$	1.93	1.56 ± 0.83	13.56 ± 1.49

parameter A is larger than its best-fit value (thus, A is compatible with zero) for all the NS masses, and the same is true for $\bar\nu_\mu$ for the largest NS mass. Additionally, the quality of the fit is similar for ν_μ and ν_τ, while it is slightly better for $\bar\nu_\tau$ compared to $\bar\nu_\mu$, since the relative error of the best-fit parameters for $\bar\nu_\tau$ is smaller. This reveals a small difference between the nonelectron flavors. As a common trend, the parameter B increases with the NS mass for all of the neutrino species.

APPENDIX E: FURTHER DETAILS ON THE IMPACT OF CONVECTION AND MUONS

Here we give further details on the impact of convection and muons. Since models 1.62-SFHx-c and 1.61-LS220-c

stop before the product tL_{ν_i} for all neutrino species is reduced to a value of 0.15 of the maximum, to make the comparison on a solid ground in this Appendix we consider data up to $t_{\nu_i,c}$ for simulations with DD2 and SFHo and up to $t_{\nu_i,Co}$ for simulations with SFHx and LS220 (see Appendix A for more details). In this way, we take into account results for neutrinos and antineutrinos of all flavors up to the time when they reach the same reduction factor. Moreover, since nonelectron flavors show, in general, a similar behavior and in simulations without muons, τ and μ neutrinos behave *exactly* in the same way, for all the simulations considered in this Appendix we report values related only to ν_e, $\bar\nu_e$, ν_μ, and $\bar\nu_\mu$.

We list the best-fit parameter values and their 1σ errors for the $1.62M_\odot$ models with different EOS and different ingredients of the input physics for the luminosities of neutrinos in Table X and of antineutrinos in Table XI. A better visualization of the change in the best-fit parameters can be obtained by plotting them as a function of the PNS mass for the different EOSs. As an example, we show in Fig. 16 the best-fit parameters for $\bar\nu_e$ as a function of M_{NS}, for DD2 (left panels) and SFHo (right panels). Here, black dots are the values of the best-fit parameters obtained from simulations including both convection and muons, red dots are related to simulations without convection, and blue dots to simulations without muons.

Tables X and XI, as well as Fig. 16, show that, as a general trend, in simulations without convection τ becomes larger and n smaller, i.e., the luminosity suppression starts at later times and it is slower. The only exception is found for $\tau_{\bar\nu_e}$ in model 1.62-DD2-c, which is smaller than $\tau_{\bar\nu_e}$ in 1.62-DD2 (see the red dot in the third panel from top on the left of Fig. 16). This behavior is confirmed by inspecting the upper left panel in Fig. 13, where the orange line (without convection) is peaked at earlier times compared to the blue (benchmark case) and the green (without muons) lines. As shown by the upper left panel in Fig. 14, even if $\tau_{\bar\nu_e}$ is smaller than in the benchmark case, the fit well reproduces the data, because the interplay between $\tau_{\bar\nu_e}$ and a much smaller $n_{\bar\nu_e}$ (compared to the complete case) well describes the slightly longer cooling time. Therefore, for $\bar\nu_e$ we observe a mathematical peculiarity connected to the fit function, reacting to the fact that $tL_{\bar\nu_e}$ is peaked at earlier times in the absence of convection (see the upper left panel in Fig. 13), i.e., smaller $\tau_{\bar\nu_e}$, and it is characterized by a milder exponential suppression, i.e., smaller n, leading to a longer cooling time. On the other hand, in the absence of convection α becomes smaller in the case of DD2 (see the red dot in the second panel from top on the left of Fig. 16) and larger in the case of SFHo (see the red dot in the second panel from top on the right of Fig. 16), describing a change in the power-law behavior in the early cooling phase. In all the cases, the best-fit parameters in the absence of convection lie well outside the 1σ confidence band found for

TABLE X. Best-fit parameter values for $L_{\nu_i} = C t^{-\alpha} e^{-(t/\tau)^n}$ for ν_e (left) and $\bar\nu_e$ (right) for $M_{\mathrm{NS}} = 1.62 M_\odot$ and different EOS, considering both convection and muons (upper lines), without convection (labeled with the suffix -c), and without muons (labeled with the suffix -m). We consider data up to $t_{\nu_i,c}$ for simulations with DD2 and SFHo and up to $t_{\nu_i,\mathrm{Co}}$ for simulations with SFHx and LS220 (see Appendix A for more details). Simulations with SFHx and LS220 without muons are not available.

Model	C_{ν_e} (B/s)	α_{ν_e}	τ_{ν_e} (s)	n_{ν_e}	$C_{\bar\nu_e}$ (B/s)	$\alpha_{\bar\nu_e}$	$\tau_{\bar\nu_e}$ (s)	$n_{\bar\nu_e}$
1.62-DD2	7.040 ± 0.010	0.430 ± 0.002	6.319 ± 0.004	3.959 ± 0.008	8.260 ± 0.014	0.529 ± 0.002	6.538 ± 0.004	4.599 ± 0.012
1.62-DD2-c	5.746 ± 0.008	0.190 ± 0.003	6.713 ± 0.019	1.763 ± 0.005	6.705 ± 0.008	0.157 ± 0.004	5.920 ± 0.022	1.594 ± 0.005
1.62-DD2-m	7.194 ± 0.010	0.479 ± 0.002	6.211 ± 0.003	5.208 ± 0.011	8.737 ± 0.009	0.567 ± 0.001	6.300 ± 0.002	5.443 ± 0.009
1.62-SFHo	8.308 ± 0.005	0.601 ± 0.001	7.743 ± 0.002	3.639 ± 0.003	8.967 ± 0.008	0.612 ± 0.001	7.823 ± 0.003	3.971 ± 0.005
1.62-SFHo-c	6.780 ± 0.009	0.625 ± 0.001	12.60 ± 0.01	2.347 ± 0.005	8.025 ± 0.012	0.720 ± 0.002	12.87 ± 0.02	2.367 ± 0.006
1.62-SFHo-m	8.713 ± 0.007	0.654 ± 0.001	7.493 ± 0.002	4.305 ± 0.005	9.128 ± 0.006	0.581 ± 0.001	7.265 ± 0.002	3.945 ± 0.004
1.62-SFHx	8.479 ± 0.003	0.6552 ± 0.0003	8.049 ± 0.001	4.045 ± 0.002	9.692 ± 0.004	0.7127 ± 0.0005	8.209 ± 0.001	4.544 ± 0.004
1.62-SFHx-c	6.433 ± 0.007	0.550 ± 0.001	11.97 ± 0.02	1.859 ± 0.004	7.488 ± 0.009	0.608 ± 0.002	11.87 ± 0.03	1.736 ± 0.005
1.62-LS220	306.2 ± 71.4	-0.679 ± 0.063	0.044 ± 0.011	0.394 ± 0.011	305.5 ± 56.9	-0.702 ± 0.052	0.051 ± 0.010	0.406 ± 0.009
1.61-LS220-c	7.426 ± 0.005	0.878 ± 0.001	16.64 ± 0.01	2.779 ± 0.003	9.013 ± 0.007	1.013 ± 0.001	17.31 ± 0.01	2.942 ± 0.005

TABLE XI. Best-fit parameter values for $L_{\nu_i} = C t^{-\alpha} e^{-(t/\tau)^n}$ for ν_μ (left) and $\bar\nu_\mu$ (right) for $M_{\mathrm{NS}} = 1.62 M_\odot$ and different EOS, considering both convection and muons (upper lines), without convection (labeled with the suffix -c), and without muons (labeled with the suffix -m). We consider data up to $t_{\nu_i,c}$ for simulations with DD2 and SFHo and up to $t_{\nu_i,\mathrm{Co}}$ for simulations with SFHx and LS220 (see Appendix A for more details). Simulations with SFHx and LS220 without muons are not available.

| Model	C_{ν_μ} (B/s)	α_{ν_μ}	τ_{ν_μ} (s)	n_{ν_μ}	$C_{\bar\nu_\mu}$ (B/s)	$\alpha_{\bar\nu_\mu}$	$\tau_{\bar\nu_\mu}$ (s)	$n_{\bar\nu_\mu}$
1.62-DD2	8.428 ± 0.011	0.430 ± 0.002	6.595 ± 0.003	4.542 ± 0.009	9.271 ± 0.012	0.486 ± 0.001	6.676 ± 0.003	4.569 ± 0.009
1.62-DD2-c	6.831 ± 0.010	0.282 ± 0.002	8.025 ± 0.014	2.209 ± 0.005	7.406 ± 0.010	0.274 ± 0.002	7.635 ± 0.015	2.060 ± 0.005
1.62-DD2-m	8.780 ± 0.007	0.474 ± 0.001	6.407 ± 0.001	5.669 ± 0.007	9.174 ± 0.007	0.482 ± 0.001	6.406 ± 0.001	5.708 ± 0.007
1.62-SFHo	9.669 ± 0.008	0.582 ± 0.001	8.104 ± 0.003	4.022 ± 0.005	10.60 ± 0.01	0.633 ± 0.001	8.239 ± 0.002	4.094 ± 0.003
1.62-SFHo-c	8.394 ± 0.012	0.686 ± 0.001	14.53 ± 0.01	3.288 ± 0.007	9.037 ± 0.013	0.702 ± 0.001	14.31 ± 0.01	3.120 ± 0.007
1.62-SFHo-m	9.939 ± 0.003	0.5920 ± 0.0004	7.712 ± 0.001	4.320 ± 0.002	10.407 ± 0.003	0.6002 ± 0.0004	7.713 ± 0.001	4.344 ± 0.002
1.62-SFHx	10.00 ± 0.01	0.638 ± 0.001	8.427 ± 0.002	4.462 ± 0.004	11.125 ± 0.005	0.6887 ± 0.0004	8.540 ± 0.001	4.305 ± 0.003
1.62-SFHx-c	7.988 ± 0.011	0.645 ± 0.001	14.88 ± 0.01	2.736 ± 0.006	8.603 ± 0.011	0.664 ± 0.001	14.76 ± 0.01	2.647 ± 0.006
1.62-LS220	439.5 ± 123.0	-0.624 ± 0.074	0.040 ± 0.012	0.388 ± 0.012	494.5 ± 139.4	-0.785 ± 0.077	0.043 ± 0.013	0.404 ± 0.012
1.61-LS220-c	10.05 ± 0.01	0.950 ± 0.001	16.87 ± 0.01	2.526 ± 0.004	10.82 ± 0.01	0.976 ± 0.001	16.81 ± 0.01	2.540 ± 0.004
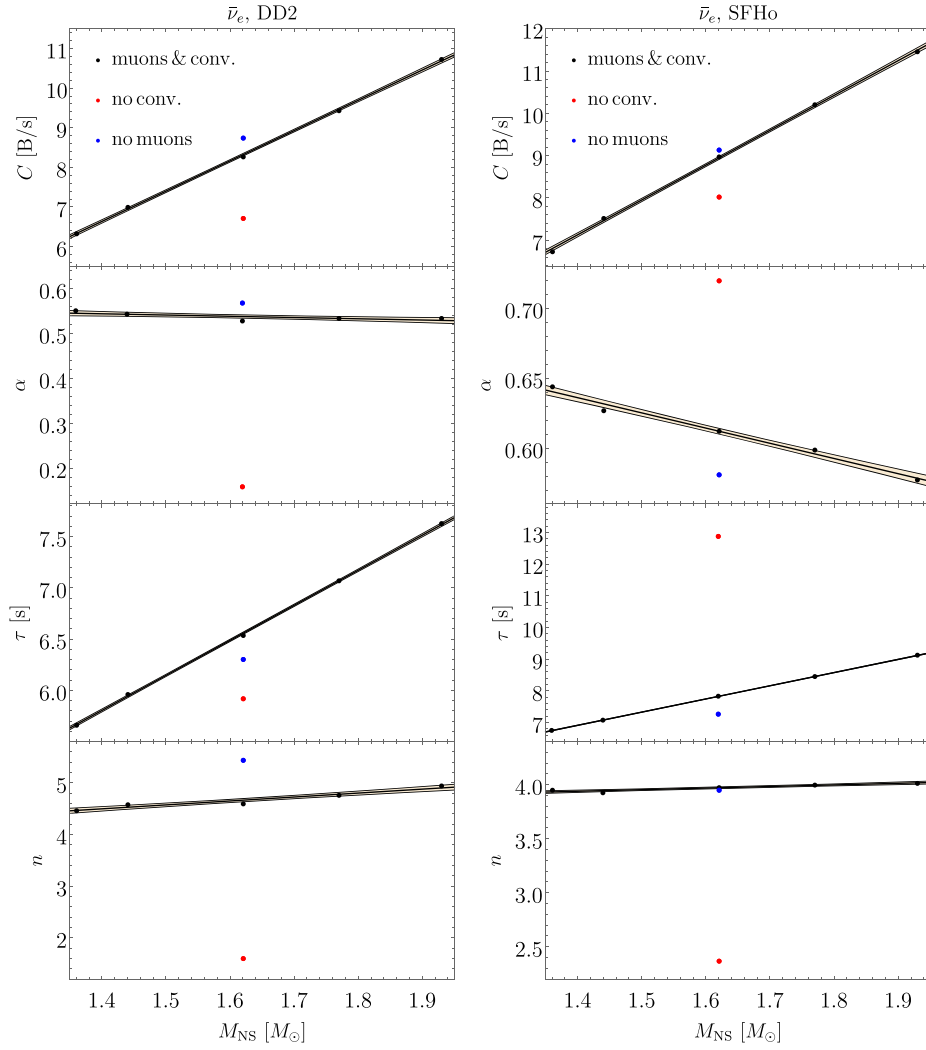
FIG. 16. Best-fit parameters C, α, τ, and n as functions of the PNS mass for $\bar{\nu}_e$ and DD2 (left), respectively, SFHo (right), with data up to $t_{\bar{\nu}_e,c}$. The shaded areas represent the 1σ confidence bands. The black dots are obtained with simulations considering both convection and muons, red dots neglect convection, whereas blue dots correspond to simulations without muons.

benchmark simulations, stressing the strong impact of convection on the neutrino signal.

The weaker impact of muons on the neutrino signal is highlighted by the small changes in the best-fit parameters obtained from simulations without muons. In this case, for both DD2 and SFHo, in simulations without muons τ becomes slightly lower and n is approximately equal or slightly larger for neutrinos and antineutrinos of all flavors (compare the first with the third line in the first two data blocks of Tables X and XI, as well as the black and blue dots in Fig. 16). This means that in simulations without muons the suppression in the luminosity starts slightly before and it is a bit faster than in the full-physics cases. In contrast, α tends to increase for DD2 and to decrease for SFHo, even if the change in all cases is much smaller compared to the changes induced by the absence of convection.

Since simulations without muons are not available for SFHx and LS220 and for them $X_{\nu_i}^{\text{fin}} > 0.15$ in the absence of convection, we do not show the best-fit parameter values as a function of the NS mass in these two cases, but we only summarize the values of the best-fit parameters and their errors in the last two data blocks of Table X (for the electron flavor) and Table XI (for the muon flavor), obtained by considering simulation data up to $t_{\nu_i,\text{Co}}$. Even if the nominal values of the best-fit parameters in the benchmark simulations slightly change when switching from $t_{\nu_i,c}$ to $t_{\nu_i,\text{Co}}$, the impact of convection on simulations with SFHx and SFHo is similar, with an increase in τ, and a decrease in C and in n in absence of convection. As expected, convection strongly affects also simulations with LS220. In this case, given the worse quality of the fit, neglecting convection leads to completely different values of the best-fit parameters compared to the benchmark case. Indeed, simulations

without convection show positive values of α, much larger values of τ and n, and drastically reduced values of C compared to the complete-physics case, with all of these parameter values more closely related to the true magnitude and exponential decay time of the neutrino luminosities.

APPENDIX F: EQUATION-OF-STATE PARAMETERS

We report in Table XII the parameters for the symmetry energies for the EOS cases used in our work. With the customary definitions of $x = (n - n_0)/(3n_0)$ and the asymmetry parameter $\delta = 1 - 2Y_e$, the energy per nucleon can be expressed as

$$E(n) = -E_0 + \frac{1}{2}Kx^2 + \delta^2\left(J + Lx + \frac{1}{2}K_s x^2\right) + \cdots,$$

$$(F1)$$

TABLE XII. Parameter values for the energy per nucleon around the nuclear saturation density n_0 according to Eq. (F1) for the EOSs used in the model simulations in our work. The values in this table are taken from Table IV in [67] and from entries for the respective EOS in the CompOSE database [68].

EOS	n_0 (fm^{-3})	E_0 (MeV)	K (MeV)	J (MeV)	L (MeV)	K_s (MeV)
DD2	0.149	16.0	243	31.7	55.0	−93.2
SFHo	0.158	16.2	245	31.6	47.1	−205
SFHx	0.160	16.2	239	28.7	23.2	−40.0
LS220	0.155	16.0	220	28.6	74.0	−24.0

with E_0 being the binding energy of symmetric matter at saturation density, K the incompressibility, J the symmetry energy, L the slope of the symmetry energy, and K_s the curvature of the symmetry energy.

[1] K. Scholberg, Supernova neutrino detection, Annu. Rev. Nucl. Part. Sci. **62,** 81 (2012).

[2] A. Mirizzi, I. Tamborra, H.-T. Janka, N. Saviano, K. Scholberg, R. Bollig, L. Hüdepohl, and S. Chakraborty, Supernova neutrinos: Production, oscillations and detection, Riv. Nuovo Cimento **39,** 1 (2016).

[3] K. Nakamura, S. Horiuchi, M. Tanaka, K. Hayama, T. Takiwaki, and K. Kotake, Multimessenger signals of long-term core-collapse supernova simulations: Synergetic observation strategies, Mon. Not. R. Astron. Soc. **461,** 3296 (2016).

[4] L. F. Roberts and S. Reddy, Neutrino signatures from young neutron stars, arXiv:1612.03860.

[5] S. Horiuchi and J. P. Kneller, What can be learned from a future supernova neutrino detection?, J. Phys. G **45,** 043002 (2018).

[6] F. An et al. (JUNO Collaboration), Neutrino physics with JUNO, J. Phys. G **43,** 030401 (2016).

[7] R. F. Lang, C. McCabe, S. Reichard, M. Selvi, and I. Tamborra, Supernova neutrino physics with xenon dark matter detectors: A timely perspective, Phys. Rev. D **94,** 103009 (2016).

[8] K. Abe et al. (Hyper-Kamiokande Collaboration), Supernova model discrimination with Hyper-Kamiokande, Astrophys. J. **916,** 15 (2021).

[9] A. Ankowski et al., Supernova Physics at DUNE, in Supernova Physics at DUNE (2016), arXiv:1608.07853.

[10] B. Abi et al. (DUNE Collaboration), Supernova neutrino burst detection with the Deep Underground Neutrino Experiment, Eur. Phys. J. C **81,** 423 (2021).

[11] A. S. Dighe, M. T. Keil, and G. G. Raffelt, Detecting the neutrino mass hierarchy with a supernova at IceCube, J. Cosmol. Astropart. Phys. 06 (2003) 005.

[12] I. Tamborra, F. Hanke, B. Müller, H.-T. Janka, and G. Raffelt, Neutrino signature of supernova hydrodynamical instabilities in three dimensions, Phys. Rev. Lett. **111,** 121104 (2013).

[13] B. Müller, Neutrino emission as diagnostics of core-collapse supernovae, Annu. Rev. Nucl. Part. Sci. **69,** 253 (2019).

[14] H. Nagakura, A. Burrows, D. Vartanyan, and D. Radice, Core-collapse supernova neutrino emission and detection informed by state-of-the-art three-dimensional numerical models, Mon. Not. R. Astron. Soc. **500,** 696 (2020).

[15] S. Shibagaki, T. Kuroda, K. Kotake, and T. Takiwaki, Characteristic time variability of gravitational-wave and neutrino signals from three-dimensional simulations of non-rotating and rapidly rotating stellar core-collapse, Mon. Not. R. Astron. Soc. **502,** 3066 (2021).

[16] H. Nagakura, A. Burrows, and D. Vartanyan, Supernova neutrino signals based on long-term axisymmetric simulations, Mon. Not. R. Astron. Soc. **506,** 1462 (2021).

[17] H. Nagakura and D. Vartanyan, Efficient method for estimating the time evolution of the proto-neutron star mass and radius from a supernova neutrino signal, Mon. Not. R. Astron. Soc. **512,** 2806 (2022).

[18] Z. Lin, S. Zha, E. P. O'Connor, and A. W. Steiner, Detectability of neutrino-signal fluctuations induced by the hadron-quark phase transition in failing core-collapse supernovae, Phys. Rev. D **109,** 023005 (2024).

[19] N. K. Largani, T. Fischer, and N. U. F. Bastian, Constraining the onset density for the QCD phase transition with the neutrino signal from core-collapse supernovae, Astrophys. J. **964,** 143 (2024).

[20] I. Tamborra and S. Shalgar, New developments in flavor evolution of a dense neutrino gas, Annu. Rev. Nucl. Part. Sci. **71,** 165 (2021).

[21] M. C. Volpe, Neutrinos from dense environments: Flavor mechanisms, theoretical approaches, observations, and new directions, Rev. Mod. Phys. **96,** 025004 (2024).

[22] B. Dasgupta, Collective neutrino oscillations: Beginning and end, *Proc. Sci.*, NOW2022 (2023) 083.

[23] F. Capozzi and N. Saviano, Neutrino flavor conversions in high-density astrophysical and cosmological environments, Universe **8,** 94 (2022).

[24] M. Sen, Supernova neutrinos: Flavour conversion mechanisms and new physics scenarios, Universe **10,** 238 (2024).

[25] G. Raffelt and P. Muenchen Supernova as particle-physics laboratory, in *Hamburg Neutrinos from Supernova Explosions* (Verlag Deutsches Elektronen-Synchrotron, Hamburg, 2011), pp. 59–64, 10.3204/DESY-PROC-2011-03/raffelt.

[26] A. Caputo and G. Raffelt, Astrophysical axion bounds: The 2024 edition, *Proc. Sci.*, 454 (2024) 041 [arXiv:2401 .13728].

[27] M. T. Keil, G. G. Raffelt, and H.-T. Janka, Monte Carlo study of supernova neutrino spectra formation, Astrophys. J. **590,** 971 (2003).

[28] I. Tamborra, B. Müller, L. Hüdepohl, H.-T. Janka, and G. Raffelt, High-resolution supernova neutrino spectra represented by a simple fit, Phys. Rev. D **86,** 125031 (2012).

[29] T. Totani, K. Sato, H. E. Dalhed, and J. R. Wilson, Future detection of supernova neutrino burst and explosion mechanism, Astrophys. J. **496,** 216 (1998).

[30] G. L. Fogli, E. Lisi, A. Mirizzi, and D. Montanino, Probing supernova shock waves and neutrino flavor transitions in next-generation water-Cerenkov detectors, J. Cosmol. Astropart. Phys. 04 (2005) 002.

[31] A. Abusleme *et al.* (JUNO Collaboration), Real-time monitoring for the next core-collapse supernova in JUNO, J. Cosmol. Astropart. Phys. 01 (2024) 057.

[32] L. Köpke (IceCube Collaboration), Supernova neutrino detection with IceCube, J. Phys. Conf. Ser. **309,** 012029 (2011).

[33] T. J. Loredo and D. Q. Lamb, Bayesian analysis of neutrinos observed from supernova SN-1987A, Phys. Rev. D **65,** 063002 (2002).

[34] G. Pagliaroli, F. Vissani, M. L. Costantini, and A. Ianni, Improved analysis of SN1987A antineutrino events, Astropart. Phys. **31,** 163 (2009).

[35] J. F. Beacom and P. Vogel, Mass signature of supernova muon-neutrino and tau-neutrino neutrinos in Super-Kamiokande, Phys. Rev. D **58,** 053010 (1998).

[36] J. Gava, J. Kneller, C. Volpe, and G. C. McLaughlin, A dynamical collective calculation of supernova neutrino signals, Phys. Rev. Lett. **103,** 071101 (2009).

[37] R. Abbasi *et al.* (IceCube Collaboration), IceCube sensitivity for low-energy neutrinos from nearby supernovae, Astron. Astrophys. **535,** A109 (2011); **563,** C1(E) (2014).

[38] G. G. Raffelt, Stars as laboratories for fundamental physics: The astrophysics of neutrinos, axions, and other weakly interacting particles (1996), https://ui.adsabs.harvard.edu/ abs/1996slfp.book.....R.

[39] S. E. Woosley, J. R. Wilson, G. J. Mathews, R. D. Hoffman, and B. S. Meyer, The r process and neutrino heated supernova ejecta, Astrophys. J. **433,** 229 (1994).

[40] S. W. Li, L. F. Roberts, and J. F. Beacom, Exciting prospects for detecting late-time neutrinos from core-collapse supernovae, Phys. Rev. D **103,** 023016 (2021).

[41] Y. Suwa, A. Harada, K. Nakazato, and K. Sumiyoshi, Analytic solutions for neutrino-light curves of core-collapse supernovae, Prog. Theor. Exp. Phys. **2021,** 013E01 (2021).

[42] L. F. Roberts, G. Shen, V. Cirigliano, J. A. Pons, S. Reddy, and S. E. Woosley, Proto-neutron star cooling with convection: The effect of the symmetry energy, Phys. Rev. Lett. **108,** 061103 (2012).

[43] D. F. G. Fiorillo, M. Heinlein, H.-T. Janka, G. Raffelt, E. Vitagliano, and R. Bollig, Supernova simulations confront SN 1987A neutrinos, Phys. Rev. D **108,** 083040 (2023).

[44] A. Pascal, J. Novak, and M. Oertel, Proto-neutron star evolution with improved charged-current neutrino-nucleon interactions, Mon. Not. R. Astron. Soc. **511,** 356 (2022).

[45] M. Rampp and H.-T. Janka, Radiation hydrodynamics with neutrinos: Variable Eddington factor method for core collapse supernova simulations, Astron. Astrophys. **396,** 361 (2002).

[46] R. Buras, M. Rampp, H.-T. Janka, and K. Kifonidis, Two-dimensional hydrodynamic core-collapse supernova simulations with spectral neutrino transport. 1. Numerical method and results for a 15 solar mass star, Astron. Astrophys. **447,** 1049 (2006).

[47] H.-T. Janka, Explosion mechanisms of core-collapse supernovae, Annu. Rev. Nucl. Part. Sci. **62,** 407 (2012).

[48] R. Bollig, H. T. Janka, A. Lohs, G. Martinez-Pinedo, C. J. Horowitz, and T. Melson, Muon creation in supernova matter facilitates neutrino-driven explosions, Phys. Rev. Lett. **119,** 242702 (2017).

[49] Garching core-collapse supernova research archive, https:// wwwmpa.mpa-garching.mpg.de/ccsnarchive//.

[50] S. Typel, G. Röpke, T. Klähn, D. Blaschke, and H. H. Wolter, Composition and thermodynamics of nuclear matter with light clusters, Phys. Rev. C **81,** 015803 (2010).

[51] M. Hempel and J. Schaffner-Bielich, A statistical model for a complete supernova equation of state, Nucl. Phys. **A837,** 210 (2010).

[52] M. Hempel, T. Fischer, J. Schaffner-Bielich, and M. Liebendörfer, New equations of state in simulations of core-collapse supernovae, Astrophys. J. **748,** 70 (2012).

[53] A. W. Steiner, M. Hempel, and T. Fischer, Core-collapse supernova equations of state based on neutron star observations, Astrophys. J. **774,** 17 (2013).

[54] J. M. Lattimer and D. F. Swesty, A generalized equation of state for hot, dense matter, Nucl. Phys. **A535,** 331 (1991).

[55] Y. Fukuda *et al.* (Super-Kamiokande Collaboration), The Super-Kamiokande detector, Nucl. Instrum. Methods Phys. Res., Sect. A **501,** 418 (2003).

[56] K. Abe *et al.*, Calibration of the Super-Kamiokande detector, Nucl. Instrum. Methods Phys. Res., Sect. A **737,** 253 (2014).

[57] I. Tamborra, G. Raffelt, F. Hanke, H.-T. Janka, and B. Müller, Neutrino emission characteristics and detection opportunities based on three-dimensional supernova simulations, Phys. Rev. D **90,** 045032 (2014).

[58] A. Strumia and F. Vissani, Precise quasielastic neutrino/ nucleon cross-section, Phys. Lett. B **564,** 42 (2003).

[59] K. Abe *et al.* (Hyper-Kamiokande Collaboration), Hyper-Kamiokande design report, arXiv:1805.04163.

[60] K. Nakazato and H. Suzuki, Cooling timescale for proto-neutron stars and properties of nuclear matter: Effective mass and symmetry energy at high densities, Astrophys. J. **878,** 25 (2019).

[61] H.-T. Janka, Neutrino from SN 1987 A: Can they tell even more?, in *Astro-Particle Physics*, edited by A. Weiss, G. Raffelt, W. Hillebrandt, and F. von Feilitzsch (Technische Universität München, Germany, 1996) p. 154.

[62] R. Akaho, H. Nagakura, and T. Foglizzo, Detectability of late-time supernova neutrinos with fallback accretion onto protoneutron star, Astrophys. J. **960,** 116 (2024).

[63] J. Ehring, S. Abbar, H.-T. Janka, G. Raffelt, and I. Tamborra, Fast neutrino flavor conversion in core-collapse supernovae: A parametric study in 1D models, Phys. Rev. D **107,** 103034 (2023).

[64] J. Ehring, S. Abbar, H.-T. Janka, G. Raffelt, and I. Tamborra, Fast neutrino flavor conversions can help and hinder neutrino-driven explosions, Phys. Rev. Lett. **131,** 061401 (2023).

[65] T. Fischer, P. Carenza, B. Fore, M. Giannotti, A. Mirizzi, and S. Reddy, Observable signatures of enhanced axion emission from protoneutron stars, Phys. Rev. D **104,** 103012 (2021).

[66] A. Harada, Y. Suwa, M. Harada, Y. Koshio, M. Mori, F. Nakanishi, K. Nakazato, K. Sumiyoshi, and R. A. Wendell, Observing supernova neutrino light curves with Super-Kamiokande. IV. Development of SPECIAL BLEND: A new public analysis code for supernova neutrinos, Astrophys. J. **954,** 52 (2023).

[67] M. Oertel, M. Hempel, T. Klähn, and S. Typel, Equations of state for supernovae and compact stars, Rev. Mod. Phys. **89,** 015007 (2017).

[68] CompOSE—CompStar Online Supernovae Equations of State.